Remote Sensing of Environment 171 (2015) 261–277

Contents lists available at ScienceDirect

Remote Sensing of Environment

journal homepage: www.elsevier.com/locate/rse

Sea level monitoring and sea state estimate using a single geodetic receiver

Nicolas Roussel [a,b,*], Guillaume Ramillien [a,b], Frédéric Frappart [a,b], José Darrozes [a,b], Adrien Gay [b], Richard Biancale [a,b,c], Nicolas Striebig [b,d], Vincent Hanquiez [e], Xavier Bertin [f], Damien Allain [g]

[a] Université Paul Sabatier, CNRS, IRD, GET-OMP, 31400 Toulouse, France
[b] Groupe de Recherche en Géodésie Spatiale, 31400 Toulouse, France
[c] Centre National d'Etudes Spatiales, 31400 Toulouse, France
[d] Groupe d'Instrumentation Scientifique, OMP, 31400 Toulouse, France
[e] Université de Bordeaux, CNRS, UMR 5805 EPOC, 33615 Pessac, France
[f] Université de la Rochelle, CNRS, UMR 7266 LIENSs, 17000 La Rochelle, France
[g] Laboratoire d'Etudes en Géophysique et Océanographie Spatiales, OMP, 31400 Toulouse, France

ARTICLE INFO

Article history:
Received 26 May 2015
Received in revised form 8 October 2015
Accepted 21 October 2015
Available online xxxx

Keywords:
GNSS-R
SNR
Multipaths
Remote sensing
Sea level
Wave and tide gauge

ABSTRACT

GNSS-Reflectometry (GNSS-R) altimetry has demonstrated a strong potential for sea level monitoring. Interference Pattern Technique (IPT) based on the analysis of the Signal-to-Noise Ratio (SNR) estimated by a GNSS receiver, presents the main advantage of being applicable everywhere by using a single geodetic antenna and receiver, transforming them to real tide gauges. Classical SNR analysis method used to estimate the variations of the reflecting surface height $h(t)$ has a limited domain of validity due to its variation rate $\frac{dh}{dt}(t)$ assumed to be negligible. We present here a significant advance in this altimetric methodology using GNSS multipath to conjointly estimate $h(t)$ and $\frac{dh}{dt}(t)$ over areas characterized by high amplitudes of tides and presence of waves. It drastically enhances the temporal and spatial monitoring of tides and waves. Inversion approach is based on a Least Square Method (LSM), combining simultaneous measurements from different GNSS constellations (GPS, GLONASS). Our method is validated with SNR data acquired on an offshore site of 60-meter height, in conditions were assumptions of the classical SNR analysis method are not valid (i.e. with a semi-diurnal tide amplitude of ~4 m, vertical velocity of the sea surface due to tide reaching 0.2 mm/s, and presence of waves with amplitude up to few meters). Linear correlation between the estimates with our method and tide gauges records are better than 0.97, whereas it only equals 0.82 with the classical method over the whole 3 months of acquisition. Our dynamic SNR method allows a very good estimate of the main tide periods and permits to detect swell and waves with realistic amplitudes and periods, which is not the case with tide gauges (located in protected areas) or classical SNR analysis method.

1. Introduction

Coastal areas concentrate most of the economic activities and urbanization around the world. 37% of the world population was living in a band of one hundred kilometer width along the coast in 1997 (Cohen et al., 1997) and the rate of population growth in coastal areas is accelerating and increasing tourism adds pressure on the environment (UN, 2010). Although coastal ecosystems are among the most productive in the world, they are also highly threatened (Duraiappah et al., 2005). Coastal areas will be exposed to increasing natural hazards in the coming years, such as storms and sea level rise that will cause floods, erosion, ecosystem losses, human, social and economic issues (Nicholls et al., 2007). Although radar altimetry is a powerful technique used for the monitoring of the sea surface topography over the open ocean (e.g., Ablain, Cazenave, Valladeau, and Guinehut (2009)) and the study of the ocean circulation (e.g., Le Traon and Morrow (2001)), its use is difficult close to the coasts as its spatial and temporal resolutions are inadequate to observe the complex and fast changing dynamics of the ocean close to the shore (e.g., Bouffard et al. (2011)). For the same reason, radar altimetry is unable to provide information on swell and waves with a sufficient spatio-temporal sampling. A new technique known as GNSS Reflectometry (GNSS-R) and based on the analysis of the GNSS signals reflecting on the sea surface appeared during the last decades. Spatio -and/or temporal- variations of sea levels were recorded with an accuracy of a few cm using such a technique from ground-based or air-borne acquisitions (e.g., Lowe et al., 2002; Ruffini, Soulat,

* Corresponding author at: OMP, Bureau H137 — PAE, 14 Avenue Edouard Belin, 31400 Toulouse, France.
E-mail addresses: nicolas.roussel@get.obs-mip.fr (N. Roussel), guillaume.ramillien@get.obs-mip.fr (G. Ramillien), frederic.frappart@get.obs-mip.fr (F. Frappart), jose.darrozes@get.obs-mip.fr (J. Darrozes), adrien.gay.3@gmail.com (A. Gay), richard.biancale@cnes.fr (R. Biancale), nicolas.striebig@obs-mip.fr (N. Striebig), v.hanquiez@epoc.u-bordeaux1.fr (V. Hanquiez), xavier.bertin@univ-lr.fr (X. Bertin), damien.allain@legos.obs-mip.fr (D. Allain).

http://dx.doi.org/10.1016/j.rse.2015.10.011
0034-4257/

Caparrini, Germain, & Martin-Neira, 2004; Löfgren, Haas, Scherneck, & Bos, 2011; Semmling et al., 2011; Rius et al., 2012).

Interference Pattern Technique (IPT) for altimetric applications have first been reported by Anderson (1995). Cardellach, Ao, de la Torre Juarez, and Haji (2004) also used interferometric patterns to infer surface height from Low Earth Orbiter, based on both phase and Signal-to-Noise Ratio (SNR) measurements. GNSS-R tide gauge is a concept based on the use of either a single antenna which will assess GNSS reflected signals through SNR measurement, or two antennas: the first one up-looking to track the direct signal, and the second one down-looking to record the reflected signal. We propose here a significant improvement of the first method based on the analysis of the SNR of a classical geodetic antenna (Larson et al., 2008), which drastically improves the temporal and spatial monitoring of tides and waves.

Our study is presented in four main parts. The first section is a state of the art of the GNSS-R techniques, mostly focusing on the SNR-based retrieval of sea surface height. A more detailed presentation of the various GNSS-R applications can be found in Cardellach et al. (2011). Section 3 presents the dynamic SNR method we use to retrieve water levels from SNR data in extreme conditions where classical method cannot be used. This dynamic SNR method is tested with in situ data and Section 4 describes the experimental setup and ground truth data generated during the experimental campaign. Last section analyzes the results of this campaign by comparing them to independent data used as validation.

2. State of the art

2.1. GNSS-R techniques

The Global Navigation Satellites System (GNSS) provides autonomous geo-spatial positioning with global coverage thanks to more than 50 satellites from different constellations (the American Global Positioning System GPS, the Russian GLObalnaïa NAvigatsionnaïa Sistéma GLONASS,...) emitting continuously L-band microwave signals. Along with the space segment development (Galileo advent, COMPASS-Beidou development,...), the processing techniques have also been widely improved, with a better understanding and consideration of the various sources of error in the processing. Among them, multipaths still remain one of the major problems that degrade the accuracy of GNSS measurements, and the mitigation of their influence has been widely investigated (e.g., Bilich, 2006). Previous studies show that multipaths can be related to properties of the reflecting surface Martin-Neira, 1993. This opportunistic remote sensing technique, known as GNSS reflectometry (GNSS-R), is based on the analysis of the electromagnetic signals emitted continuously by the GNSS satellites and detected by a receiver after reflection on the Earth's surface. The time delay between the reception of the direct and reflected signals is directly correlated to the difference in height between the receiver and the reflecting surface. This information can be retrieved analyzing the temporal evolution of the reflected signal power known as waveforms through code- (e.g., Carreno-Luengo, Camps, Ramos-Perez, & Rius, 2014; Yu, Rizos, & Dempster, 2014) and phase-delay measurements (e.g., Semmling et al., 2012; Treuhaft, Lowe, Zuffada, & Chao, 2001). One of the major advantage of such a technique is the dense spatial and temporal coverage of the reflection points (e.g., Roussel et al., 2014), which is not only limited to a single measurement point or a non-repetitive transect as what is classically done using GNSS-equipped buoys. With the development of the geo-positioning applications, the GNSS constellations become denser and denser and a guarantee of service is ensured for the next decades.

Previous studies showed that the best accuracy is obtained with the waveforms analysis through phase-delay measurement (e.g., Treuhaft et al., 2001). Nevertheless, phase-delay measurements are only possible if the reflection is coherent. This will not work in general from airborne altitudes (or higher) over the Ocean but only over smooth sea-ice, ice sheets, and some calm water. The inversion algorithms to retrieve the receiver height from waveforms for a given epoch require a significant computing power with a huge amount of data to analyze. Interference Pattern Technique (Anderson, 1995), applied to the SNR analysis, provides, in theory, slightly worse results but the data treatment is simpler and a single classical GNSS receiver and antenna is sufficient for acquisition (Larson, Löfgren, & Haas, 2013; Löfgren, 2014).

2.2. SNR analysis: classical method

While major part of the emitted signal is received directly in the zenith-looking hemisphere of the antenna, a minor part of it comes from below the horizon, after one or several reflections in the surrounding environment (Fig. 1). These so-called multipath signals interfere with the direct wave and affect the GNSS measurements recorded by the receiver by adding new frequencies. Geodetic GNSS antennae are thus designed to reduce the contribution of the multipath which degrade the accuracy of the position determination. A typical example of this type of antenna is the "choke ring" antenna which drastically reduces multipath signals that come from near or below the horizon by reflecting them thanks to frequency-tuned rings.

Classical GNSS antennae also use the polarization properties of the GNSS signals to filter out part of the reflected waves. The waves emitted by GNSS satellites are L-band microwaves (e.g. $L1_{GPS} = 1575.42$ MHz, $L2_{GPS} = 1227.60$ MHz) and Right-Hand Circularly Polarized (RHCP). But its polarization may change upon reflection depending on the reflector type (i.e., reflection coefficient) and the incidence angle (the angle at which the signal reaches the reflector). For satellite elevation angles below a particular value named Brewster angle (8° for sea water according to Hannah, 2001), the predominant signal component after reflection is the co-polar, or the RHCP, and hence the result is right-hand elliptical polarization. Conversely, for elevation angles greater than the Brewster angle, the predominant signal component is the cross-polar, or LHCP, and hence the result is left-hand elliptical polarization. GNSS geodetic antennas are thus designed to attenuate LHCP signals to reduce effects of multipaths. GNSS antennas radiation pattern focuses the antenna gain for RHCP signals towards zenith and decreases the gain with decreasing elevation angle.

These filtering techniques affect the total received signal by reducing the reflected signals amplitude with respect to the direct signal amplitude. It is however well-known that the energy of the reflected signal is not completely dampened. The lower the satellite elevation angle is, the larger the contribution of the reflected signal is.

The effect of multipath reflection clearly affects SNR data recorded by GNSS receivers (Löfgren, 2014) on the different frequencies:

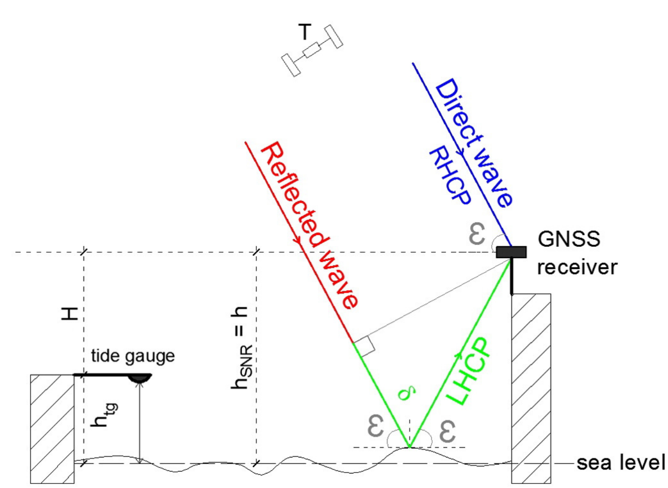

Fig. 1. Principle of GNSS tide gauge using a single GNSS antenna. ε : satellite elevation angle, δ: additional path covered by the reflected way (green line). (For interpretation of the references to color in this figure legend, the reader is referred to the web version of this article.)

e.g., on L1 C/A code (S1C) or L2 precise code (S2P) for instance. SNR can be related to the coherent addition of direct and reflected GNSS signals in the receiving antenna.

Following Larson et al. (2008), instantaneous SNR is described by:

$$SNR^2 = A_d^2 + A_m^2 + 2A_dA_m\cos(\psi) \quad (1)$$

where A_m and A_d are the amplitudes of the multipath and direct signal respectively, and ψ the phase difference between the two signals. Since (i) GNSS antennas are designed to filter reflected signals, and (ii) the reflected signal is attenuated upon reflection, we can assume that $A_m \ll A_d$. SNR can thus be approximated by:

$$SNR^2 \approx A_d^2 + 2A_dA_m\cos(\psi) \quad (2)$$

Eq. (2) shows that overall magnitude of the SNR is large and mainly driven by the direct signal. The reflected signal will affect the SNR by producing a high frequency associated with small amplitude perturbation w.r.t the direct signal. The reflected signal perturbations will mainly be visible for low satellite elevation angles (Löfgren et al., 2011).

According to Bishop and Klobuchar (1985) and Georgiadou and Kleusberg (1988), and assuming a planar reflector which corresponds to sea water, the relative phase angle can be derived geometrically from the path delay δ of the reflected signal:

$$\psi = \frac{2\pi}{\lambda}\delta = \frac{4\pi h}{\lambda}\sin(\varepsilon) \quad (3)$$

with λ the signal wavelength, ε the satellite elevation and h the distance between the antenna phase centre and the reflecting surface (i.e. the receiver height): see Fig. 1. From Eq. (3) it is possible to derive the frequency of the multipath oscillations:

$$f_\psi = \frac{d\psi}{dt} = \frac{4\pi\dot{h}}{\lambda}\sin(\varepsilon) + \frac{4\pi h}{\lambda}\cos(\varepsilon)\,\dot{\varepsilon} \quad (4)$$

$\dot{h}$ $(=\frac{dh}{dt})$ defines the vertical velocity and $\dot{\varepsilon}$ $(=\frac{d\varepsilon}{dt})$ defines the elevation angle velocity. Eq. (4) can be simplified by making a change of variable $x = \sin(\varepsilon)$. We thus obtain:

$$\tilde{f} = \frac{d\psi}{dx} = \frac{4\pi}{\lambda}\left(\dot{h}\,\frac{\tan(\epsilon)}{\dot{\epsilon}} + h\right) \quad (5)$$

Eq. (5) shows that, in a static or quasi- static case ($\dot{h} \simeq 0$), this frequency $\tilde{f}$ of the multipath oscillation is constant and directly proportional to the receiver height above the reflecting surface. Measuring $\tilde{f}$ variations can lead to determine h, the antenna height above the receiving surface, and thus to the sea surface variations for each time interval. Nevertheless, if $\dot{h}$ can not be neglected, the frequency depends on the satellite elevation angle ε, the satellite elevation angle velocity $\dot{\varepsilon}$, as well as the vertical velocity between the antenna and the reflecting surface $\dot{h}$. If the two former terms are known, the knowledge of $\dot{h}$ is an important parameter and must be considered as unknown in most cases. This situation leads to an under-determined system of equations. Most of the SNR studies conducted until now were done in conditions such as $\dot{h}$ could be neglected (Larson et al., 2013; Löfgren, Haas, & Scherneck, 2014). For instance, when Löfgren and Haas (2014) compared sea level solutions from SNR and phase-delay analysis in a fjord where only tides are sensitive, the change in the receiver height was around a few tens of centimeters over 3 days of observation, and $\dot{h}$ was then negligible from an instant to another. However, in many cases, this assumption is not reasonable due to waves with significant height which make $\dot{h}$ drastically increase. High tide amplitudes over a short period of time is also susceptible to produce high $\dot{h}$ values. Löfgren et al. (2014) suggested to take $\dot{h}$ into account by doing two iterations: the first one neglecting it and the second one integrating an estimation of $\dot{h}$ from sinusoidal functions fitted to the reflector height series obtained with the first iteration. The underlying idea was that, during one day, the most significant contribution to the changes in sea level height comes from the diurnal and semi-diurnal tides with known frequencies. This method increased the accuracy of the results, however it needs a previous knowledge of the phenomenon susceptible to influence the receiver height in the region under study. Larson et al. (2013) proposed a similar method, also based on two iterations: the first iteration is done determining h without integrating $\dot{h}$; $\dot{h}$ is then estimated from this coarse $h(t)$ time series to produce height corrections. Unfortunately, this method can only work for small $\dot{h}$ values and not for measurement sites with significant waves for instance (e.g., offshore sea level measurements). In our study, we propose a new method to simultaneously estimate h and $\dot{h}$ (see Section 3): the dynamic SNR method. Our approach will be tested in the conditions of important sea surface variations (i.e., SNR measurements made at the top of an offshore lighthouse), where both tides and waves are present and the assumption of $\dot{h}$ being negligible is not satisfied (see Section 4.1).

3. General form of the dynamic SNR method

This section presents the methodology developed to simultaneously estimate h and $\dot{h}$ when facing important dynamic cases ($\dot{h} \neq 0$). The methodology is based on the determination of the time series $\tilde{f}(t)$ of the frequency of the multipath oscillations from the SNR data of each GNSS satellite. Using the $\tilde{f}(t)$ of several satellites visible at the same time, it is possible to build an over-determined equations system based on Eq. (5) considering only two unknown parameters: h and $\dot{h}$. Such a linear system of equations can be solved using a classical Least Square Method (LSM) adjustment.

This algorithm of estimation is detailed hereafter, and is composed of four main steps presented in a flow chart in Fig. 2:

1. Preprocessing and removal of the direct signal contribution in the raw SNR observations.
2. Windowing and optimization of the moving windows parameters.

Determination of the frequency of the multipath oscillations $\tilde{f}(t)$ from the reduced SNR time series by harmonic analysis.

Determination of $h(t)$ conjointly to $\dot{h}(t)$, that are directly linked to the sea level (Fig. 1).

3.1. Preprocessing and removal of the direct signal contribution

Due to hardware cutoff in conventional geodetic receivers, SNR is not continuously estimated (or not) as the same sampling as the data used for positioning. Hence many records are missing in the SNR time series. To reduce these effects, the following conditions are imposed:

- length of the SNR time series needs to be greater than 300 s.
- SNR data are temporally interpolated when the gaps in the record are lower than 10 s. If SNR values are missing over a longer time period, they are processed as two distinct independent sequences.
  These values were adjusted experimentally to provide lowest Mean Squared errors in the results from the LSM resolution criteria (see Section 3.4).

As presented in Fig. 2, the direct signal is more powerful in the SNR time series for a long time period and corresponds to the main low frequency, whereas the multipath signals cause small amplitude perturbations at high and medium frequencies. To determine the frequency

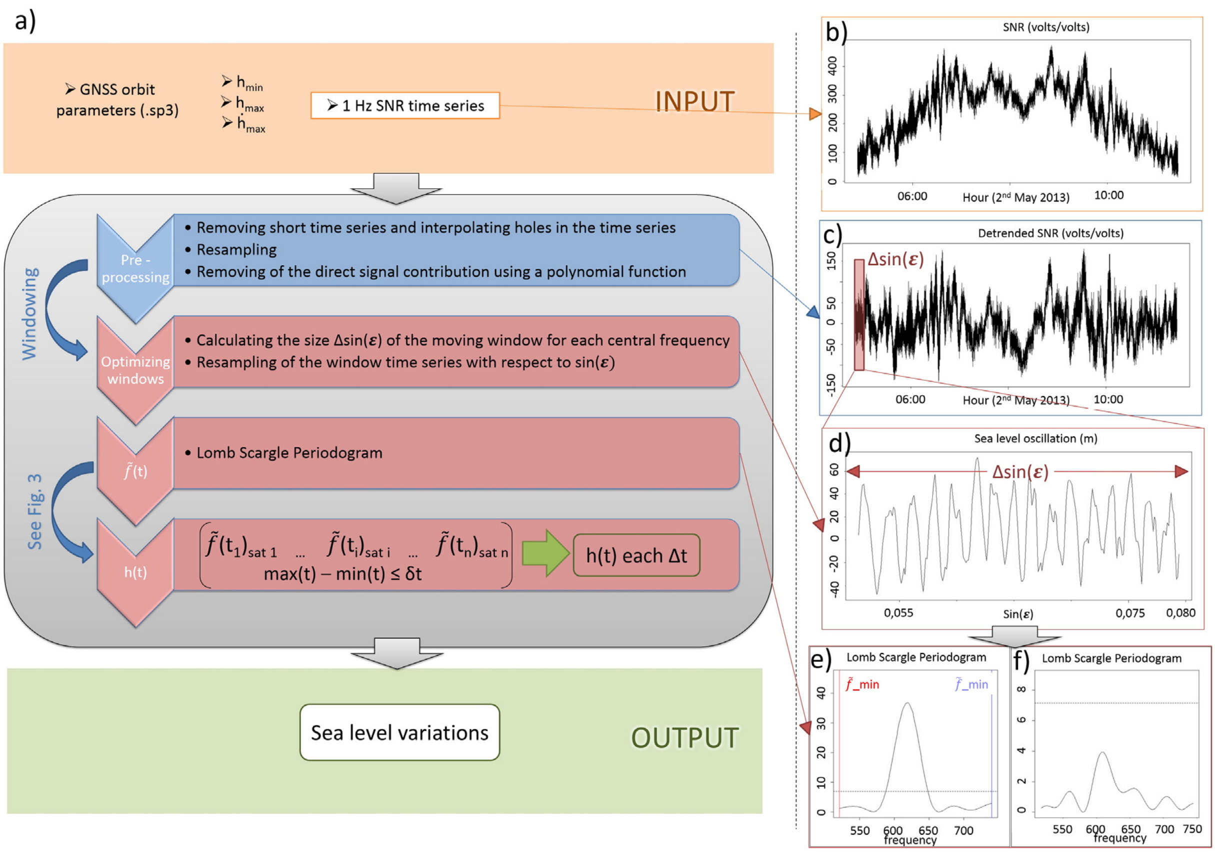

Fig. 2. Processing chain. Time series are from the GPS satellite PRN23 the 2nd May 2013. a) Flow chart presenting the processing of the SNR data: the input, the different steps of the processing, and the output; b) Example of raw SNR data time series (input); c) Example of SNR detrended data time-series; d) Zoom on SNR detrended data against sin(ε); e) and f) Examples of Lomb-Scargle Periodograms of the SNR detrended data. (e) The LSP presents a peak ranging between f_{min} and f_{max} and reaching statistical significance at an error probability equal to 0.01 (Ruf, 1999). (f) The LSP does not present a peak reaching statistical significance at an error probability equal to 0.01 (Ruf, 1999) and is thus rejected.

$\tilde{f}(t)$ of the multipath oscillations necessary to solve Eq. (5), this direct signal contribution must be removed from the raw SNR profile. Bilich (2006) proposed to remove the direct signal effect through gain pattern modeling. This method requires the knowledge of the gain patterns of both the receiving antenna of the GNSS receiver and the emitting antenna of the GNSS satellite. As the information is difficult to obtain, Larson et al. (2008) suggested to fit a simple low-order polynomial to the SNR time series and to substract it from the starting SNR data to isolate the variations due to multipath. As this later method yields better results than the modeling one (Bilich, 2006), we adopted it and removed a second-order polynomial from the SNR time series.

3.2. Windowing of the time series

The frequency of the multipath oscillations $\tilde{f}(t)$ in the SNR time series is determined using a Lomb Scargle Periodogram: LSP (Lomb, 1976; Scargle, 1982) computed with a moving window of 5 min width (see Section 3.3). Five minutes correspond to the classical tide gauges sampling (see §2.4). The analysis is not directly performed on $SNR = f(t)$ but on $SNR = f(\sin(\varepsilon))$ as in Eq. (5).

The choice of the length of the moving window is critical as it should be large enough to get a precise determination of $\tilde{f}(t)$. But the size of the analysis window must not be too large so that the frequency of the oscillations remains quasi-constant over this window. Let $\Delta(\sin\varepsilon)$ be the size of the moving-average window. To find the suited size $\Delta(\sin\varepsilon)$ around each central value, an a priori coarse knowledge of the parameters under determination is mandatory. We choose to consider the following three parameters as known by the user:

- h_{min}: the minimum height above the reflecting surface the receiver is susceptible to reach during the observation period.
- h_{max}: the maximum height above the reflecting surface the receiver is susceptible to reach during the observation period.
- $\dot{h}_{max}$: the absolute maximum vertical velocity of the reflecting surface (rate of change of the receiver height).

The more precise the knowledge of these three values is, the faster the determination of $\tilde{f}$ will be. From these three values, expected $\tilde{f}_{min}$ and $\tilde{f}_{max}$ are estimated for each central value, based on Eq. (5). In order to get the largest moving window through which the frequency could be considered as constant, and to describe enough variations of SNR within the chosen window, the following two conditions are considered:

$$\frac{\Delta\tilde{f}_{max}}{\tilde{f}_{min}} \le p \tag{6}$$

$$\frac{N_0}{\tilde{f}_{min}} < \Delta(\sin(\varepsilon)) \tag{7}$$

With p the maximal variation of $\tilde{f}$ (in %) accepted within the moving window, N_0 the minimal number of observed periods within the moving window (needed to get a good estimate of $\tilde{f}$), and $\Delta\tilde{f}_{max}$ is the maximal variation over time of the frequency. $\Delta\tilde{f}_{max}$ and $\tilde{f}_{min}$ will be different for each moving window because the mean elevation and elevation rate will differ for each window.

$\Delta\tilde{f}_{max}$ is computed from Eq. (5) as follows:

$$\frac{d\tilde{f}}{dt} = \frac{2}{\lambda}\left(\dot{h} + \frac{\ddot{h}\tan(\varepsilon)}{\dot{\varepsilon}} + \frac{\dot{h}}{\cos^2\varepsilon} - \frac{\dot{h}\ddot{\varepsilon}\tan\varepsilon}{\dot{\varepsilon}^2}\right) \quad (8)$$

By replacing dt by the variation of the sinus of the elevation angle we obtain:

$$\frac{d\tilde{f}}{d(\sin\varepsilon)} = \frac{d\tilde{f}}{dt}\frac{dt}{d(\sin\varepsilon)} = \frac{d\tilde{f}}{dt}\frac{1}{\dot{\varepsilon}\cos\varepsilon} \quad (9)$$

Considering the maximal value $\dot{h} = \dot{h}_{max}$ and $\ddot{h} = 0$ inside the moving window, we obtain:

$$\frac{\Delta\tilde{f}_{max}}{\Delta(\sin\varepsilon)} \leq \left|\frac{2}{\lambda\dot{\varepsilon}\cos\varepsilon}\right| \left|\left(\dot{h}_{max} + \left|\frac{\dot{h}}{\cos^2\varepsilon}\right| + \left|\frac{\dot{h}\ddot{\varepsilon}\tan\varepsilon}{\dot{\varepsilon}^2}\right|\right)\right| \quad (10)$$

We thus estimate an optimized size $\Delta(\sin\varepsilon)$ of moving-average window guaranteeing to have at least ten periods of a quasi-constant frequency. This size is not constant over the whole time series and is re-estimated for each increment.

In most of the previous studies, $\dot{h}$ was negligible and numerically neglected. But if we consider the culmination of a satellite pass, $\dot{\varepsilon}$ will tend to zero, hence the correction term $\frac{\dot{h}}{\dot{\varepsilon}\tan(\varepsilon)}$ tends to infinity, as well as the corresponding frequency $\tilde{f}$ tends to infinity. This issue was not previously settled as the parts of the time series likely to be concerned were removed when the elevation angle was above 30° or 40°. The criteria defined in the present study permits to filter the indeterminable frequencies in a systematic and far much accurate way.

3.3. Determination of the frequency $\tilde{f}$ of the multipath oscillations

After the removal of the direct signal contribution using the polynomial approach defined by Larson et al. (2008), we obtain a signal whose frequency is described by Eq. (5). The precise determination of this frequency is crucial for the determination of the sea level variations. This frequency is not stationary because of the time variations of the parameters h, $\dot{h}$, ε and $\dot{\varepsilon}$. As in recent studies (Larson et al., 2013), this dominant frequency is estimated using the LSP which seems to be a well-adapted solution. A LSP is thus applied for each moving-average window (see Section 3.2). Thanks to the knowledge of $h_{\min}$, $h_{\max}$ and $\dot{h}_{max}$, the theoretical value of $\tilde{f}_{min}$ and $\tilde{f}_{max}$ can be determined. It is thus not anymore necessary to consider the whole spectra of the signal under study, but it is sufficient to only consider frequencies between $\tilde{f}_{min}$ and $\tilde{f}_{max}$ to compute the LSP and identify the main peak. Only periodograms peaks reaching statistical significance with an error probability equals to 0.01 (Ruf, 1999) and defining a local maximum between $\tilde{f}_{min}$ and $\tilde{f}_{max}$ are retained.

3.4. Height and height change determination

Once $\tilde{f}(t)$ is accurately estimated for each satellite in sight of the receiver, *h(t)* can be obtained by inverting Eq. (5). The solution presented in this study is obtained by the combination of the measurements from all the available GNSS satellites insight at a given epoch to determine conjointly $h(t)$ and $\dot{h}(t)$ using a classical LSM resolution.

Let $\tilde{f} = \frac{d\psi}{dx}$, $U = \frac{4\pi\tan(\varepsilon)}{\lambda\dot{\varepsilon}}$, and $V = \frac{4\pi}{\lambda}$. Eq. (5) related to satellite i at the instant t becomes:

$$\tilde{f}_i(t) = U_i\dot{h}(t) + V_i h(t) \quad (11)$$

where $\tilde{f}_i(t)$ is the frequency of the multipath oscillations, with respect to the sine of the satellite elevation angle ε. Combining all the satellites visible at each moment t, a system of linear equations is obtained:

$$\begin{pmatrix} \tilde{f}_1(t) = U_1\dot{h}(t) + V_1 h(t) \\ \tilde{f}_2(t) = U_2\dot{h}(t) + V_2 h(t) \\ \tilde{f}_3(t) = U_3\dot{h}(t) + V_3 h(t) \\ \dots \end{pmatrix} \quad (12)$$

or equivalently in terms of matrix:

$$\tilde{F} = U\dot{h}(t) + Vh(t) = AX \quad (13)$$

with $A = (U\ \ V)$ and $X = \begin{pmatrix} \dot{h}(t) \\ h(t) \end{pmatrix}$.

Eq. (13) is solved with the LSM at each time step t for conjoint determination of $h(t)$ and $\dot{h}(t)$ as follows:

$$X = \left(A^tA\right)^{-1}\left(A^t\tilde{F}\right) \quad (14)$$

All GNSS satellites from the different constellations (GPS, GLONASS,...) are likely combined in this over-determined system.

The main challenge is to find the correct time interval Δt between each estimation and also the length δt of the moving window (see

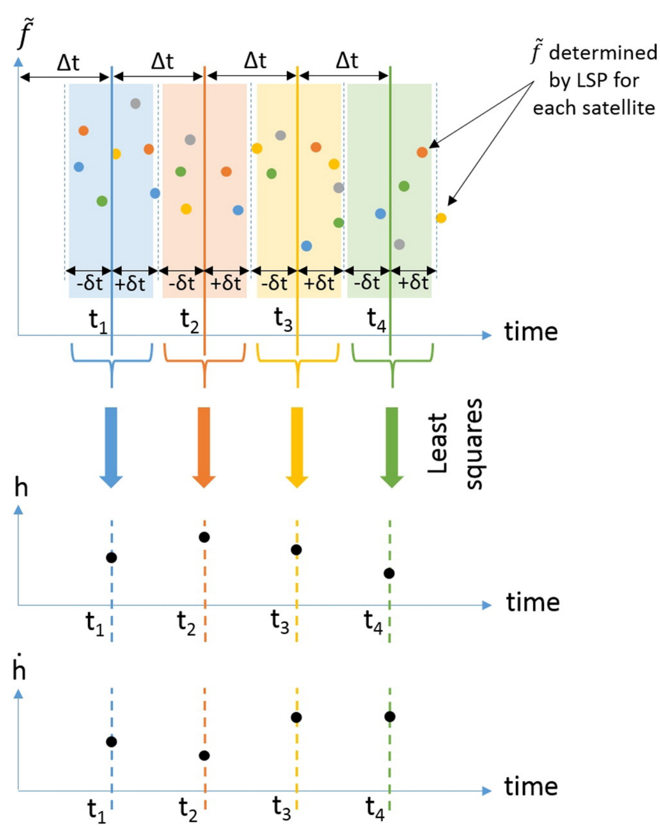

Fig. 3. Principle of the Least Squares inversion Method used to determine h and $\dot{h}$ based on LSP estimates of f. For reasons of clarity, overlapping was not represented in this figure, even if in our case δt>Δt.

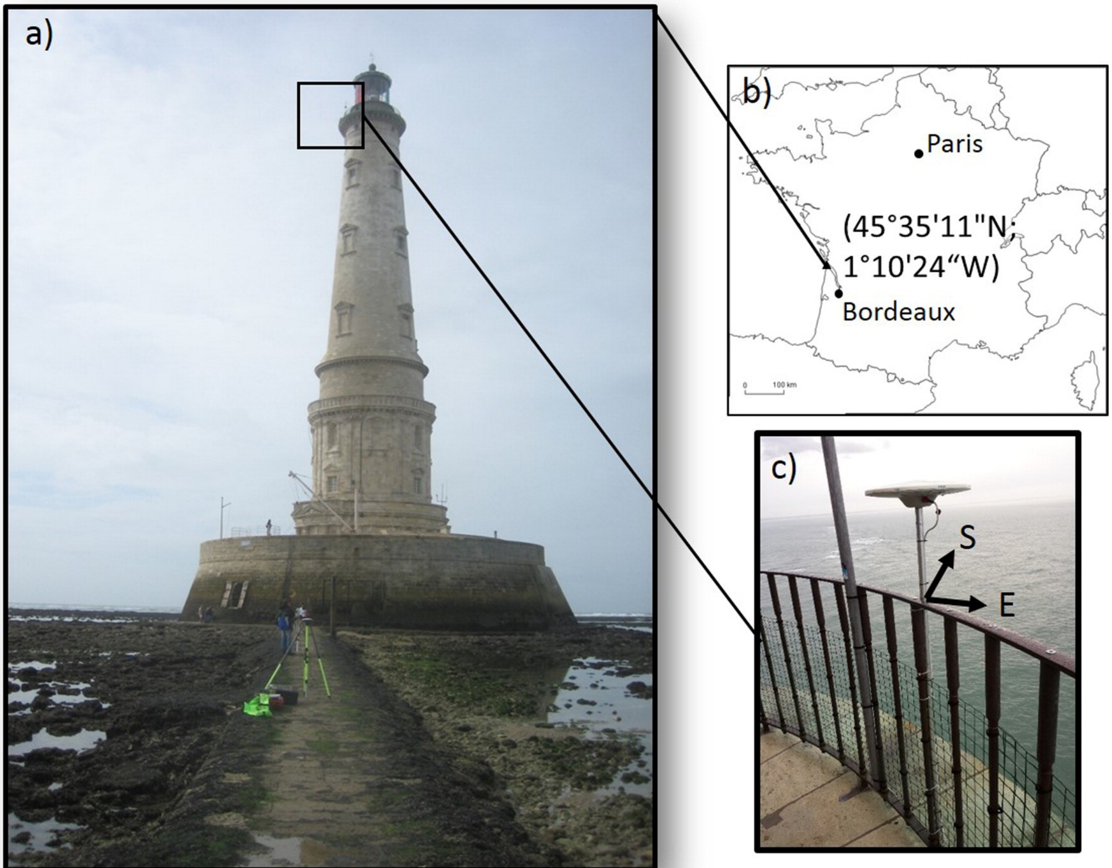

Fig. 4. Trimble Zephyr Geodetic 2 antenna with Trimble NetR9 receiver on top of Cordouan lighthouse at approx. 60 m above sea level (a). The Cordouan lighthouse (45°35′11″N; 1°10′24″W) is located at the mouth of the Gironde estuary in the South West of France (b). A Trimble NetR9 receiver with a Zephyr Geodetic 2 antenna were installed close to the top of the lighthouse (c).

Fig. 3). Δt and δt must be chosen with attention to have a large enough temporal resolution for h and $\dot{h}$.

The number of satellites observations available decreases with δt, the size of the moving window, and so the accuracy of the determination of h and $\dot{h}$ using LSM. Yet, choosing a too large value for δt causes an inaccurate determination of the unknown parameters since the receiver height would have changed during this interval due to the tide variation. The choice of δt depends on the period of the physical parameters assessed and must then be tuned to reach the best results.

3.5. Filtering of the retrieved sea level time series

As the main goal of our study is to retrieve the main astronomical tide periods (i.e., > 6 hours), the time series $h(t)$ obtained with the

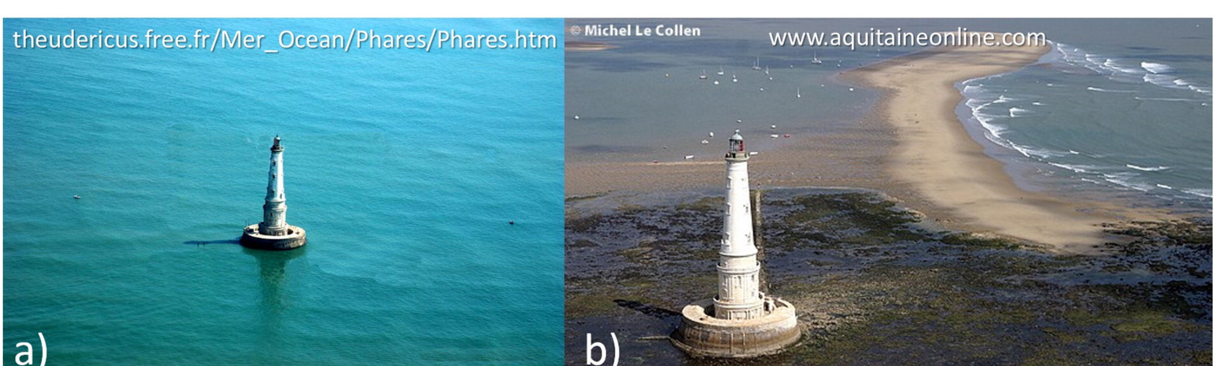

Fig. 5. Cordouan lighthouse at high tide (a) with calm sea, and low tide (b) where main sandbanks are visible.

dynamic SNR method is filtered: all periods below the minimal astronomical tide period (i.e., 6 hours) are considered as noise and removed from the time series. This is achieved by applying a second-order Butterworth low-pass filter (Butterworth, 1930).

3.6. Process validation in a static case

To validate the methodology and to reach the accuracy of the process, a Leica GR25 with an AR10 antenna were installed in the parking

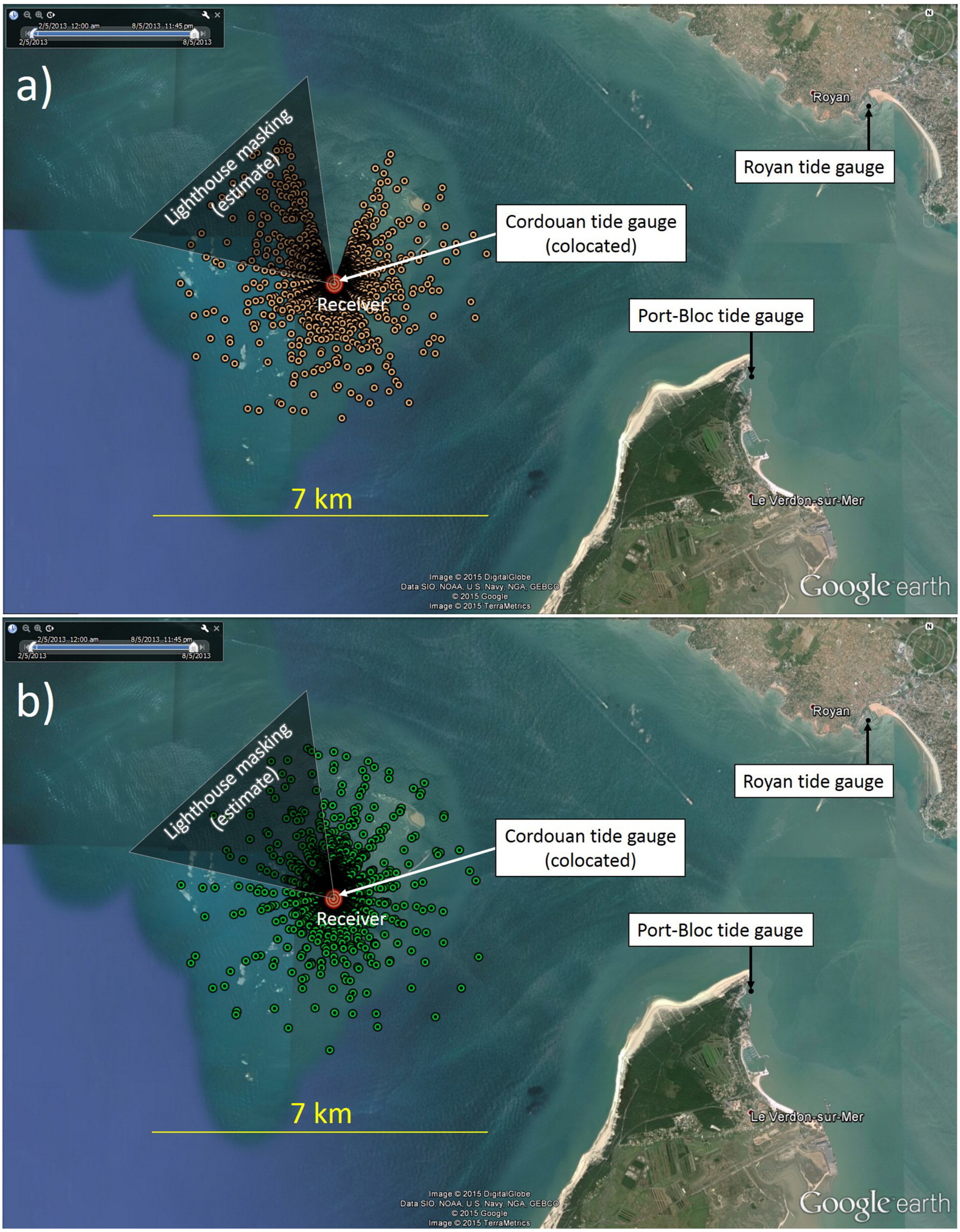

Fig. 6. Locations of the specular reflection points for a GNSS receiver on the top of the Cordouan lighthouse from 2th to 8th May 2013, considering GPS (a) and GLONASS (b) constellations. Simulation results are presented for a 15 min sampling rate (i.e., satellite positions actualized every 15 min). Only GPS (a) and GLONASS (b) satellites with elevation angles greater than 1° were considered.

lot of Observatoire Midi-Pyrénées (Toulouse, France) during four consecutive days from 12 to 15 July 2014. Data were recorded continuously with a 1 Hz frequency, and the S1C SNR data were continuously collected. The receiver height is constant and equal to 1.60 m over the whole period of measurement. Only few cars were parked during the period of acquisition, and except for a small nearby pavement (corresponding to a receiver height equal to 1.40 m), the reflecting asphalt surface can be considered as homogeneous. Only a tree masked the signals coming from the north.

Two different processes were applied to the time series considering:

- a **static SNR method (i.e., the classical method)** neglecting $\dot{h}$ as done by, e.g., Larson et al. (2013). $h(t)$ is directly retrieved from $\tilde{f}(t)$ considering the classical formula $h(t) = \frac{\lambda \tilde{f}(t)}{4\pi}$;
- a **dynamic SNR method (i.e., our new method)**. $h(t)$ is retrieved using the whole methodology presented in §2. As inputs parameters, $h_{\min}$ was set to 1.4 m (to avoid reflections on the pavement), $h_{\max}$ was set to 2 m, and $\dot{h}_{max}$ to 10^{-6} m/s (i.e. 3.6 mm/h).

The mean receiver height estimated over the whole period and considering the static case ($\dot{h} = 0$) is equal to 1.61 ± 0.10 m and 1.60 ± 0.06 m integrating the $\dot{h}$ determination. The results agree with the given uncertainties.

4. The Cordouan lighthouse experiment

4.1. The measurement site for SNR acquisition

We applied the method presented above to the SNR data acquired with a geodetic antenna set up at ~60 meters above the surface of the Atlantic ocean, at Cordouan lighthouse. Data were continuously acquired from 3 March 2013 to 31 May 2013, i.e. 3 months with the S1C SNR data routinely collected. Satellite coordinates were obtained from the IGS ephemeris final products which provide GNSS orbits with a centimetric precision and clock offset data with a temporal resolution of 15 minutes in the SP3 format for the past epochs (ftp://igs.ensg.ign.fr/pub/igs/products/).

The GNSS receiver was installed offshore at the top of the Cordouan lighthouse (45 35′11″N; 1 10′24″W) close to Le Verdon, France (Fig. 4). Cordouan lighthouse is located in the Gironde estuary at 8 km from the shore and is managed by the French "*Subdivision des Phares et Balises*" and the French "*Syndicat Mixte pour le Développement Durable de l'Estuaire de la Gironde* (*SMIDDEST*)". Typically, variations of the antenna height reached ±4 meters, and the maximum amplitude variation of the semi-diurnal tide reach 0.2 mm/s. At high tides, waves of few-meter high are also susceptible to appear. In such conditions, $\dot{h}$ could not be neglected any more and classical methods neglecting it could not be used.

The close environment around the lighthouse is really heterogeneous and varies drastically with time. Sandbanks around the lighthouse, covered during high tides, emerge as the tides recede. The major one is located between azimuth N50 and N80 s and the second one between N300 s and N330 s. Smaller sandbanks also appears at low tides in the close vicinity of the lighthouse. This particular bathymetry around the lighthouse, coupled with the current effects in the vicinity of the Gironde estuary, modifies the wave behavior around the studied area. If big waves can appear at high tides, the sea surface tends to be really calm as the tide recedes.

Fig. 5 is a photograph of the Cordouan lighthouse at high tide (a), and low tide (b) periods.

4.2. The experimental settings

We use a Trimble NetR9 receiver with a Zephyr Geodetic 2 antennae with a 50 dB ± 2 dB gain (LNA included). The Zephyr Geodetic 2 antenna has a LHCP rejection at boresight of 20 dB minimum. For further information on this Trimble receiver and antenna, please refer to NetR9 User Guide and Zephyr Geodetic 2 datasheet. GPS L1, L2, L2C, L5 frequencies and GLONASS L1 and L2 frequencies were acquired at a 1 Hz frequency with no elevation angle mask. In our study, S1C SNR is used: signal strength on L1 C/A channel (the Coarse/acquisition ranging code, freely available to the public). S1C time series is the one likely to give the best results (Löfgren & Haas, 2014) since the strength of L2 frequency signals are weaker (i.e. lower SNR) than the signals of frequency band L1.

Table 1
Coordinates of the the GNSS antenna and tide gauges used as validation.

(WGS84)	Longitude	Latitude	Ellipsoidal height (m)
GNSS antenna	1°10′24.00″W	45°35′10.66″N	107.376
Cordouan tide gauge	1°10′23.34″W	45°35′11.30″N	44.57
Royan tide gauge	1°01′40.12″W	45°37′14.07″N	43.37
Port-Bloc tide gauge	1°03′41.60″W	45°34′06.53″N	43.45

4.3. Interest of the measurement site for GNSS reflectometry

Due to its location in open ocean and its height above the sea surface (~60 m), the Cordouan lighthouse is a privileged site for GNSS-R measurements.

Accurate locations of the specular reflection points on the reflecting surface and first Fresnel zone area were determined through direct modeling using GNSS Reflected Signals Simulations (GRSS) developped by Roussel et al. (2014).

Fig. 6 shows the theoretical locations of the specular reflection points for both GPS and GLONASS satellites from the 2 May 2013 to the 8 May 2013. Farthest reflection points are a bit more than 3400 m from the receiver for satellite elevations above 1 (with a first Fresnel zone of ~20000 m^2, and reach 340 m for satellite elevations above 10 (with a first Fresnel zone of ~20000 m^2). We already highlight here one major advantage of the SNR analysis to assess the sea level with respect to the classical tide gauges: measurements are not punctual but cover a whole area around the instrument (circle with a radius of ~3.5 km for the Cordouan lighthouse).

4.4. Datasets used for validation

4.4.1. In situ tide gauges

To validate our SNR-based sea level variation estimates, we compared them to in situ records provided by classical tide gauges, all of them protected against wave effects:

- the Royan tide gauge (45 37′14.07″N; 1 01′40.12″W; 43.37 m), located at ~12 km from the Cordouan lighthouse. Records of this tide gauge are the property of MEDDE (*Ministère de l'Ecologie, du*

Table 2
Tides taken into account by the T-UGOm tide model.

Tide	Astronomic potential amplitude (cm)	Period (hours)
N2	0.6	12.9
E2	0.2	13.1
K1	14.1	23.9
K2	3.1	12.0
L2	0.7	12.2
La2	0.2	12.2
M2	24.2	12.4
M4	0.0	6.2
Mu2	0.6	12.9
N2	4.6	12.7
Nu2	0.9	12.7
O1	10.1	25.8
P1	4.7	24.1
Q1	1.9	26.9
R2	0.1	12.0
S2	11.3	12.0
T2	0.7	12.0

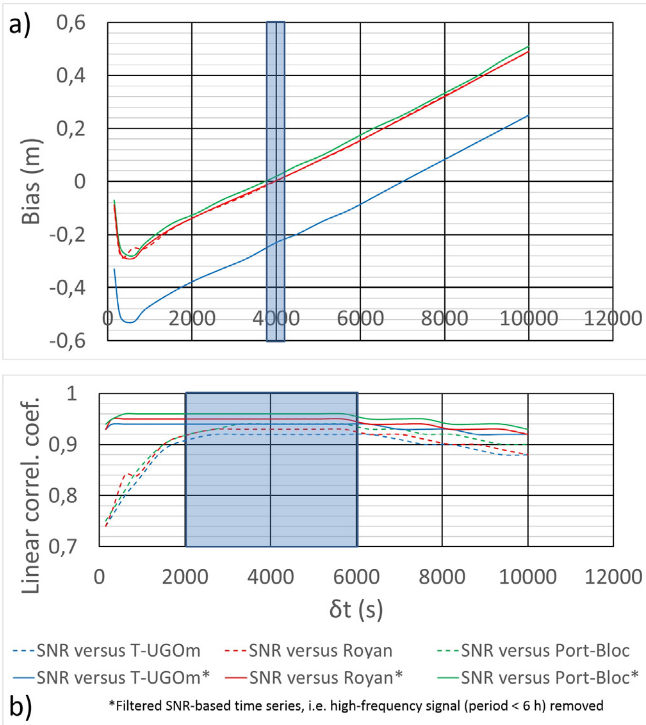

Fig. 7. Comparisons between the raw and filtered SNR-based time series and the three tide gauges over the 3 months time-series. a) Bias against δt. b) Linear correlation against δt. Blue area highlights the best results.

Développement Durable et de l'Energie), and are available on the REFMAR website (http://refmar.shom.fr). Observations are provided with a sampling frequency of 5 minutes.

- the **Port-Bloc tide gauge** (45 34′6.53″N; 1 3′41.60″W ; 43.45 m), located at ~9 km from the lighthouse. Records of this tide gauge are the property of SHOM/Bordeaux GPM. Observations are provided with a sampling frequency of 10 minutes.
- the **Cordouan lighthouse tige gauge**, located at the base of the lighthouse. Records of this tide gauge are the property of SHOM/Bordeaux GPM and we unfortunately had access to only two weeks of measurements from 28 April to 13 May 2013. Due to the absence of digital records for this tide gauge, data were extracted from scansheet scanning with ArcGIS for Desktop software (© Esri), with sampling frequency and temporal resolution of 2 minutes and 20 seconds, respectively. Ellipsoidal height of the GNSS antenna at the top of the lighthouse is 107.376 m, hence there is a height difference of 64.006 m between GNSS antenna and Royan tide gauge, and 63.926 m between GNSS antenna and Port-Bloc tide gauge. Height difference between the antenna and Cordouan tide gauge is 62.802 m.

Table 1 recapitulates the coordinates of the different points.

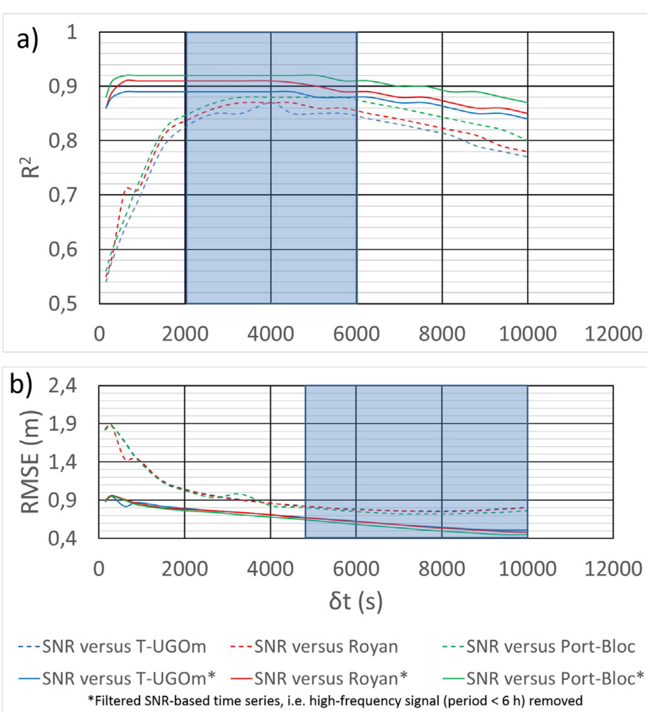

Fig. 8. Comparisons between the SNR-based time series (with and without removing high frequencies) and the three tide gauges over the 3 months time-series. a) R^2 against δt. b) RMSE against δt. Blue area highlights the best results.

Table 3
Comparison between the different tide gauges with the raw and filtered SNR-based time series over the whole 3 months of measurements, with δt = 4000s. Results are given as follows: raw SNR-based time series/filtered SNR-based time series.

SNR w.r.t.	Bias (m)	R	R^2	RMSE (m)	Shift (min)
T-UGOm	−0.23/−0.23	0.92/0.94	0.87/0.89	0.86/0.71	−4.4/−4.3
Port-Bloc	0.02/0.02	0.94/0.96	0.88/0.92	0.83/0.68	29.0/29.0
Royan	0.00/0.00	0.93/0.95	0.87/0.91	0.86/0.71	24.5/25.0

4.4.2. Tide model

The T-UGOm (*Toulouse Unstructured Grid Ocean model*) tide model developed by Lyard, Lefevre, Letellier, and Francis (2006) and based on FES2012 was also used to validate our estimates. FES2012 was used in this study for several reasons. The authors have a direct access to the expertise behind its set-up. Also, this is a coastal study, so resolution is critical. The authors had no choice but to discard really coarse resolution atlases such as 1/2 GOT4.8, so coarse it does not even reach the area of interest. The authors also have access to the original unstructured atlases, when the published FES2012 atlases are a 1/16 interpolation. FES2012 is so fine it covers even the Gironde estuary. Finally, FES2012 has been shown to be the best model over shelf regions (Stammer et al., 2014).

This theoretical astronomical model leads to the characterization of the main constituents of the tidal spectrum i.e. semidiurnal M2

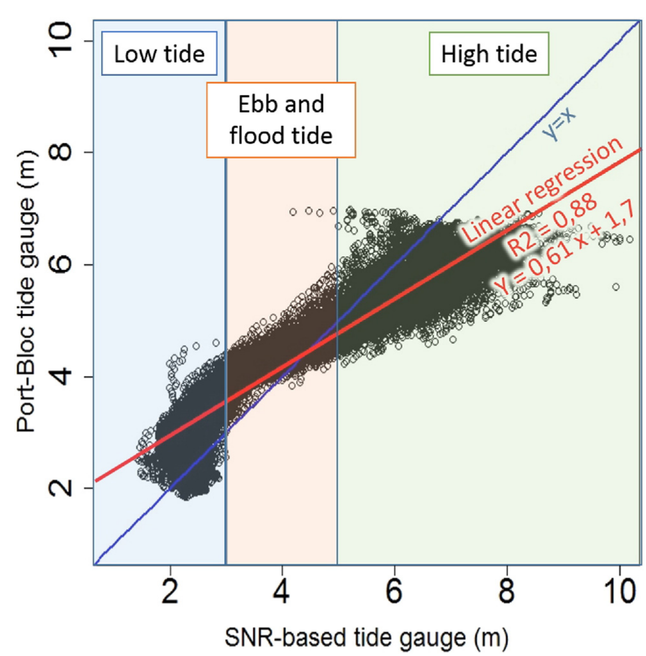

Fig. 9. Scatter plot of the raw SNR-based time series versus Port-Bloc tide gauge.

Table 4
Comparison between the different tide gauges with the raw SNR-based time series calculated with only the GPS constellation/GLONASS constellation/both constellations.

Raw SNR w.r.t.	Bias (m)	R	R^2	RMSE (m)	Shift (min)
T-UGOm	−0.20/−0.47/−0.23	0.91/0.90/0.92	0.84/0.80/0.85	0.93/1.01/0.86	−1.6/−5.0/−4.4
Port-Bloc	0.06/−0.21/0.02	0.93/0.91/0.94	0.87/0.83/0.88	0.91/0.98/0.83	31.7/27.3/29.0
Royan	0.04/−0.23/0.00	0.92/0.91/0.93	0.85/0.82/0.87	0.93/1.00/0.86	27.7/23.1/24.5

(principal lunar), S2 (principal solar), N2 (larger lunar elliptic), K2 (luni-solar); diurnal K1 (luni-solar), O1 (principal lunar) and Q1. Table 2 provides details on tidal components taken into account by the T-UGOm model.

Three main clusters of periods describing the tide are highlighted here: the first and stronger which corresponds to the main amplitude of the tide signal is centered on a period of 12 hours, the second on a period of a bit more than 24 hours, and the last and weaker at 6 hours.

4.4.3. Wave model

We use Significant Wave Height (SWH) time series computed with NOAA Wave Watch III model (Tolman, 2014). Wave Watch III is a third generation global spectral wave model, which provides estimates of wave parameters at 1-hourly intervals. The code computes the evolution of waves in space and time and has been applied at all scales from the global ocean to the coast. It solves the action balance equation as a slowly varying function of space and time and assumes that properties of the medium (like water depth, currents) and the wave energy vary on time- and space- scales much larger than a single wave. This model was used because (i) its data are freely available, and (ii) it has demonstrated its efficiency in coastal areas (e.g., Millar, Smith, & Reeve, 2007).

4.5. Parameters used for sea surface height retrieval

Δt, the time interval between each estimation of h (see Section 3.4) was chosen equal to 5 minutes, which corresponds to the temporal resolution of most of the tide gauges.

Several empirical values for p and N_0 were tested (see Section 3.2) and the values of 0.5% and 10 provide the most robust results. The mean period of the multipath contribution is equal to 32 s (with variations depending on the sinus of the satellite elevation angle). $N_0 = 10$ thus corresponds to a mean time period equal to 5.3 minutes, which is the chosen temporal resolution of the method ($\Delta t = 5$ minutes). With regards to p, values ranging between 0.1% and 5% were tested and 0.5% gives the most numerous estimations of $\tilde{f}$ for each satellite (verifying Eq. 6 and giving best significance result from LSP). With $p > 5\%$, LSP output is only noise and no fundamental frequency can be find in the signal within the moving window. Computation realized with $p = 0.5\%$ and $N_0 = 10$ gives the best linear correlation with tide gauges.

Various values of δt, the size of the moving window used to compute h (see Section 3.4), were tested, and the results are discussed in section Section 5.1.1.

4.6. Extrapolation of missing records

Continuous and regularly sampled time-series are needed to perform a wavelet analysis and for validation purposes. It is the case for the theoretical models (T-UGOm and Wave Watch III) but neither for the in situ tide gauges nor the SNR-based tide time series. Missing records were thus extrapolated using the Data-Based Mecanistic (DBM) model developed by Young (2001) in this scope. This method analyses the frequency content of any time series to extrapolate missing data using a dynamic harmonic regression analysis, with the CAPTAIN Matlab Toolbox developed by Peter Young (Taylor, Pedregal, Young, & Tych, 2006). To validate this extrapolation method, we applied it to a complete part of the Royan tide gauge time series of water level to which we manually removed some data. Results of the interpolation are presented in Fig. S1.

We then used the wavelet cross correlation and wavelet coherence toolbox for Matlab developed by Grinsted, Moore, and Jevrejeva (2004) to compute a wavelet analysis of the extrapolated time series and the original one (Fig. S2). They do not show noteworthy changes on the frequency content. RMSE between the two time series is equal to 0.038 m and maximal difference is equal to 0.28 m. These values are not negligible, but since the frequency content remains almost unchanged, we consider this method to fill the gaps as valuable and we applied it to the time series.

5. Results

5.1. Validation of the proposed inverse method

5.1.1. Comparison with T-UGOm model, port-bloc and Royan tide gauges

The method presented in Section 3.4 was applied to the whole 3-month of SNR S1C measurements from the Cordouan lighthouse for several values of δt and with $h_{min} = 50$ m, $h_{max} = 70$ m (height of the Cordouan lighthouse above sea level ~60 m) and $\dot{h}_{max} = 5 * 10^{-4}$ m/s as inputs. $\dot{h}_{max}$ was chosen approximately equal to 3 times the maximum variation of sea level observed during the lowest tide period (i.e. ~$3 * 4$ m/6 h). Waves are likely to induce faster variations of the sea surface level, but the main purpose of our study is the monitoring of the tide. Waves will nevertheless be likely to be detected, as discussed in §4.3. The output time series will be referred as *raw SNR-based time series* in the following. A second-order Butterworth low-pass filter (see Section 3.5) was then applied to the raw SNR-based time series in order to remove noise with a period smaller than the minimum tide period (i.e., 6 h). Residuals will be referred as *filtered SNR-based time series*. The consequences of this filter are discussed in the last subsection 5.5.

We estimated the bias, linear correlation R, determination coefficient R^2, Root Mean Square Error *RMSE* and phase shift between the data used for validation (classical Royan and Port-Bloc tide-gauges and T-UGOm model outputs) and the raw and filtered SNR-based time series computed with several values of δt ranging from 150 to 10000 s. Results are presented in Figs. 7 and 8.

Bias between raw and filtered SNR-based time series and the classical tide gauges is proportional to δt (except for $\delta t < 1500$ s) and reaches zero with δt ~ 4000 s. T-UGOm theoretical model follows tshe same trend but with an offset of ~23 cm. This offset is due to the model

Table 5
Comparison between the different tide gauges with the filtered SNR-based time series calculated with only the GPS constellation/GLONASS constellation/both constellations.

Filtered SNR w.r.t.	Bias (m)	R	R^2	RMSE (m)	Shift (min)
T-UGOm	−0.19/−0.46/−0.23	0.94/0.93/0.94	0.88/0.86/0.89	0.76/0.81/0.71	−1.5/−5.0/−4.3
Port-Bloc	0.06/−0.21/0.02	0.96/0.95/0.96	0.92/0.89/0.92	0.72/0.78/0.68	31.8/27.4/29.0
Royan	0.04/−0.23/0.00	0.95/0.94/0.95	0.90/0.88/0.91	0.74/0.80/0.71	27.8/23.2/25.0

Table 6
Comparisons between the different tide gauges from 28 April to 13 May 2013. Results are given as follows: raw SNR-based time series/filtered SNR-based time series.

SNR w.r.t.	Bias (m)	R	R^2	RMSE (m)	Shift (min)
T-UGOm	−0.06/−0.06	0.95/0.97	0.91/0.94	0.74/0.60	−4.1/−4.5
Port-Bloc	0.08/0.08	0.96/0.97	0.92/0.95	0.74/0.59	29.2/28.8
Royan	0.06/0.06	0.95/0.97	0.91/0.95	0.74/0.59	25.1/24.5
Cordouan	0.01/0.01	0.96/0.97	0.91/0.95	0.77/0.63	0.0/0.0

which provides accurate relative values but not true absolute ones, whereas Royan and Port-Bloc tide gauges were leveled independently and provide almost the same bias values (±2s cm). The linear variation of the bias with δt could be explained by the positive offset induced by the sandbanks emerging during low tides. The larger the size of the smoving window, the more numerous the estimations of h affected by this offset. Please note that the tropospheric delay induced on the differential path between the direct and reflected signals is neglected in our study. This effect must undoubtedly cause a slight bias on the estimations but its correction is let for further investigation.

Linear correlation is constant when removing the high frequency signal for 600≤δt≤5700 s and decreases for $\delta t < 5700$ s. With regard to the raw SNR-based time series, linear correlation coefficient increases with δt and reaches a maximum when δt is around 4000 s and decreases for higher values of δt. Results are obviously similar with R^2 values. With regard to the RMSE, it decreases with increasing values of δt for both raw and filtered SNR-based time series. The lowest values around 0.45 m for the filtered SNR-based time series and 0.72 for the raw SNR-based time series (Fig. 8) are reached for high values of δt (>7000 s). This might be understood with the fact that increasing δt smooths the time series (moving average) which explains lowest RMSE. The high-frequency variations (caused by waves and swell, see Section 5.3.2) are filtered from the SNR-based time series with increasing δt, leading to a better agreement with tidal in situ data.

To conclude, very good agreement is found for $\delta t < 1500$ s (=25 min) with a mean linear correlation above 0.92 and bias below 20 cm for both raw and filtered SNR-based time series but lowest differences (i.e. the combined highest R^2, lowest bias and lowest RMSE) are obtained with $\delta t = 4000$ s for the three comparisons (i.e. with T-UGOm model, Port-Bloc tide gauge and Royan tide gauge). Exact numerical values of comparison with $\delta t = 4000$ s are presented in Table 3. $\delta t = 4000$ s (=1.1 h) corresponds approximately to 10% of the main period of the theoretical tide (12 h). We use this value later in the following. Bias are about few millimeters by comparing the raw and filtered SNR-based time series with Royan tide gauge and 2 cm with Port-Bloc tide gauge. An offset of 23 cm is observed with T-UGOm model which is an offset inherent to the model itself. Linear correlations range between 0.94 and 0.96 for the filtered SNR-based time series and lose 0.02 with the raw SNR-based time series. R^2 values rangsse between 0.89 and 0.92 and between 0.87 and 0.88 respectively for the filtered SNR-based and raw SNR-based time series. Mean RMSE is about 0.70 m and 15 cm higher without removing the high frequency signal.

RMSE values are quite high, which might be explained by the presence of the waves detected by the SNR-method, but not by the classical tide gauges which are protected in harbor against wave effects (see Section 5.3). Besides, Cordouan lighthouse is 7 km offshore, whereas Royan and Port-Bloc tide gauges are located near coastal environment hence much sheltered.

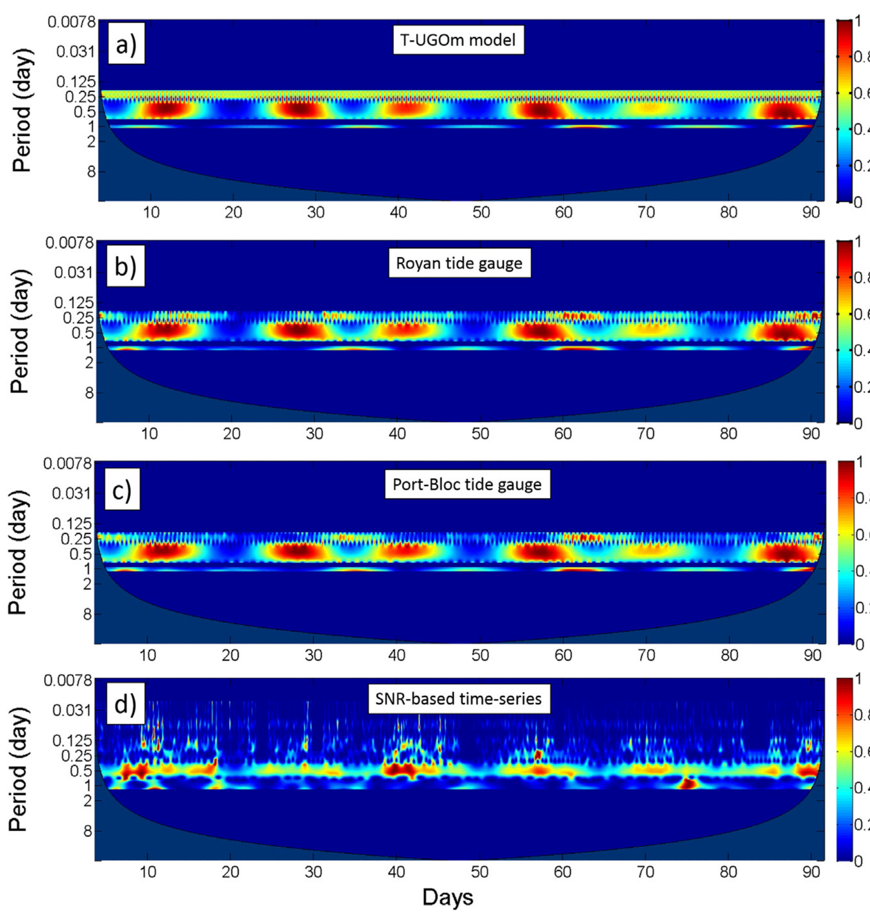

Fig. 10. Continuous wavelet transform maps: a) T-UGOm model time-series b) Royan tide gauge. c) Port-Bloc tide gauge. d) SNR-based time-series. Wavelet power is normalized between 0 and 1 for each period. A 5% significance level was calculated and only the best 99.95% results are represented. The remaining 0.05% with the worst significance level were set to 0. Abscissa is the day over the 3-month period of measurement and ordinate is the period under analysis.

Shift between SNR-based and T-UGOm time-series is about 4 minutes and is mainly due to the typical precision of the model in an estuary area. Between classical and SNR-based time-series, shifts are bigger and reach 25 minutes between SNR-based and Royan tide gauges, and 29 minutes between SNR-based and Port-Bloc tide gauges. These shifts are explained by the time of propagation of the tide covering the distance of about 10 km between them. While shift values were calculated by shifting one of the two time series until reaching best linear correlation, phase shifts will be measured in a more precise way (depending of the wave period) in Section 5.2.

Fig. 9 is the scatter plot of Port-Bloc tide time series versus raw SNR-based time series (with δt equal to 4000 s). Three main clusters appear in this scatter plot: the first one corresponds to low tides (sea level < 3 m), the second one to ebb and flood tide (sea level ranging between 3 and 5 m), and the last part which corresponds to high tides (sea level > 5 m). During high tides, SNR-based tide gauge presents higher values of sea level than Port-Bloc tide gauge. This is likely to be due to the presence of waves that are detected using the SNR-based method (see §4.3) i.e., more periods than only tides, which is not the case using tide gauge records, as they are installed in areas protected from the waves action. At low tides, SNR-based time series exhibits a lower dynamics than the Port-Bloc tide gauge due to the presence of sandbanks around the lighthouse which emerge as the tide recedes. This corresponds to no longer measurable tides (see Section 4.1). During the transition periods, at rising or falling tide, correlation between the two time series is really good and the noise increases progressively as the tides heighten, due to the augmentation of the wave amplitude.

5.1.2. Influence of the GNSS constellation

Tables 4 and 5 present the bias, linear correlation R, determination coeffsicient R^2, Root Mean Square Error (*RMSE*) and shifts between the different tide gauges and the raw and filtered SNR-based time series computed in three different cases, by considering separately:

- the satellites from the GPS constellation;
- the satellites from the GLONASS constellation;
- taking satellites from both constellations into account (i.e., the complete configuration used elsewhere in this article).

  Best results are obviously obtained when integrating the two constellations in the computations, with a linear correlation equal to 0.92 with the predicted tide (T-UGOm model), 0.94 with the Port-Bloc tide gauge data and 0.93 with the Royan tide gauge data considering the raw SNR based time series, and respectively 0.94, 0.96 and 0.95 considering the filtered SNR-based time series. Only considering GLONASS constellation leads to a decrease of the correlation of 0.01 in the three cases for the filtered SNR-based time series and up to 0.03 for the raw SNR-based time series. We do not note any significant change when only considering GPS constellation in the filtered SNR-based time series, and a decrease of 0.01 with the raw SNR-based time series.

  Considering filtered SNR-based time series, RMSE is reduced by approximately 6 cm (7 cm respectively with the raw SNR-based time series) when using only GPS constellation instead of only GLONASS constellation, and approximately 4 cm more (7 cm respectively) when combining both satellite constellations, to reach a RMSE varying between 0.68 and 0.71 m (0.83 and 0.86 m respectively). Bias are almost equal to zero when taking both constellation into account (except for the offset with T-UGOm model), ~0.22 m when only using GLONASS constellation, and ~0.05 m with GPS constellation. If GPS constellation gives better results than GLONASS constellation, results show that the more numerous the satellites are, the better the results. The use of SNR data from both constellations increases the number of available observations to solve the system of equations in (12). It also permits to increase the temporal resolution.

  These results will surely improve when new Galileo and COMPASS-Beidou constellations are added for the determination and may be also using all the other wavelengths (L2, L2C, L5, etc.). Our comparisons with independent sources of sea level variations reveal that, concerning the main tide periods, the SNR-based tide gauge provides result of similar quality to the classical tide gauges (linear correlation equal to 0.96 with Port-Bloc tide gauge for the 3-month period of test).

5.1.3. Comparison with co-located Cordouan tide gauge

Cordouan tide gauge is co-located with our GNSS receiver but its measurements are recorded on paper sheets. GPM gave us access to the records from 28 April to 13 May 2013. We thus focused on this two-week time series and compared the SNR-based measurements with the Cordouan tide gauge data over this period. Comparisons were done again during this period with the other tide gauges used as validation. Results are presented in Table 6.

The comparison with the three classical tide gauges and the T-UGOm model provides very similar results, i.e. a correlation equal to 0.97 and a RMSE value around 0.60 m with the filtered SNR-based time series. As expected, results are slightly better when removing the high-

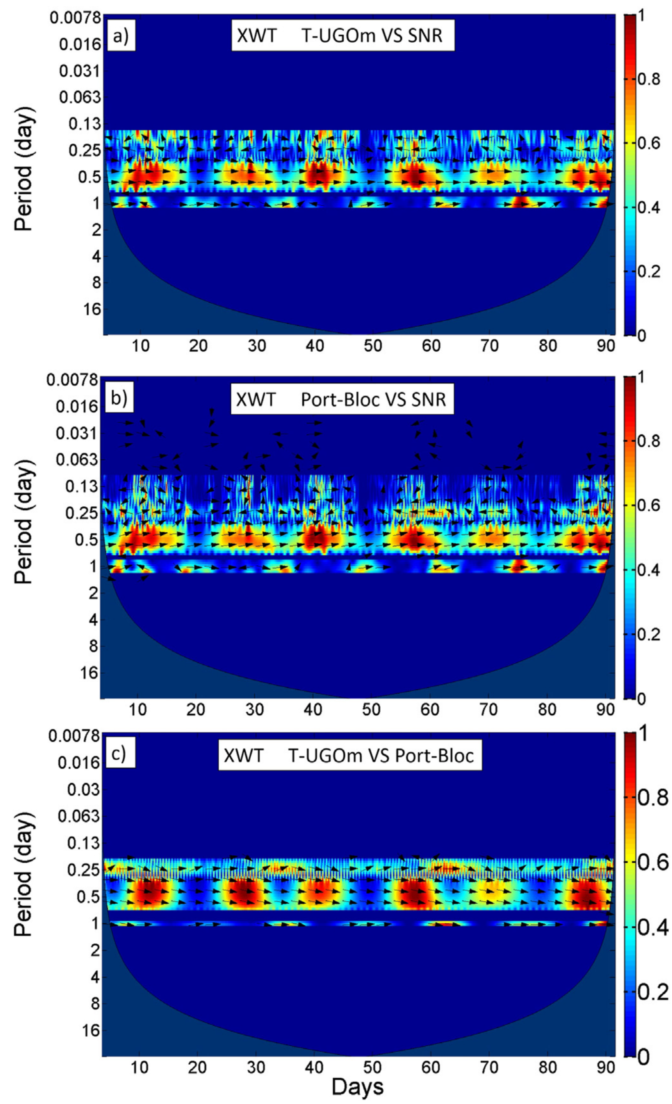

Fig. 11. Wavelet cross correlation maps: a) T-UGOm VS raw SNR. b) Port-Bloc VS raw SNR. c) T-UGOm VS Port-Bloc. Cross wavelet power in units of normalized variance. Phase arrows indicate the relative phare relationship between the series (pointing right: in-phase; left: anti-phase). Wavelet power is normalized between 0 and 1 for each period. A 5% significance level was calculated and only the best 99.95% results are represented. The remaining 0.05% with the worst significance level were set to 0. Abscissa is the day over the 3-month period of measurement and ordinate is the period under analysis.

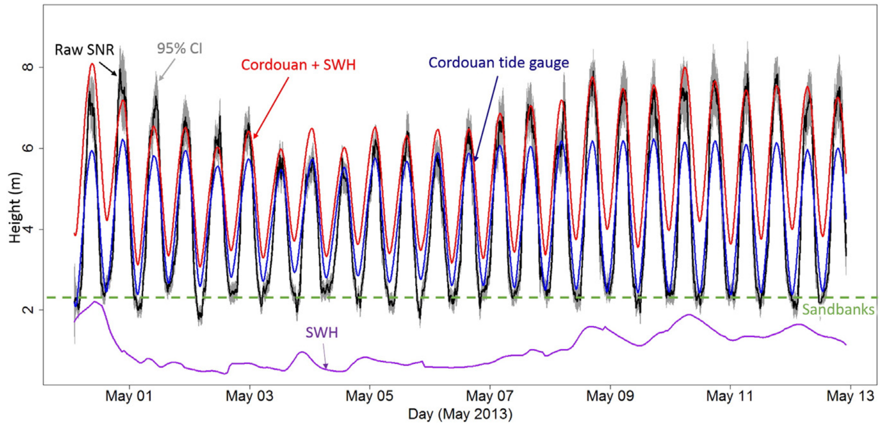

Fig. 12. Raw (black) SNR-based tide measurements compared with Cordouan tide records (blue) *plus* SWH values (red) obtained from WaveWatch III model. Gray area is the 95% Confidence Interval. Sandbanks emerge in the whole area under measurement as the tide recedes hence a minimum level at around 2.3 m. (For interpretation of the references to color in this figure legend, the reader is referred to the web version of this article.)

frequency signal, with a global increase of the linear correlation of 0.1 and mean decrease of 15 cm of the RMSE. Biases remain unchanged, and shifts almost similar. The quite high values of RMSE are due to the presence of sandbanks that emerge at low tides and of swell and waves at high tides.

5.2. Determination of the tide spectrum

A continuous wavelet transform based on Morlet mother function was applied to Royan, Port-Bloc, T-UGOm, and raw SNR-based 3-month tide time series (Fig. 10) using the wavelet toolbox for Matlab developed by Grinsted et al. (2004).

Three main periods clearly appear in the results of the wavelet transform of the predicted time series from T-UGOm (Fig. 10 a) centered on 6 hours (wave M4), 12 hours (waves N2, E2, K2, L2, La2, M2, Mu2, Nu2, R2, S2 and T2) and 24 hours (waves K1, O1, P1 and Q1) with similar intensities. These three main periods are also clearly visible on Royan and Port-Bloc time series (Fig. 10b and c). The 12-hour period is clearly visible on the raw SNR-based time series (Fig. 10 d). With regard to the 6- and 24-hour ones, they are also detected but appear much noisier than

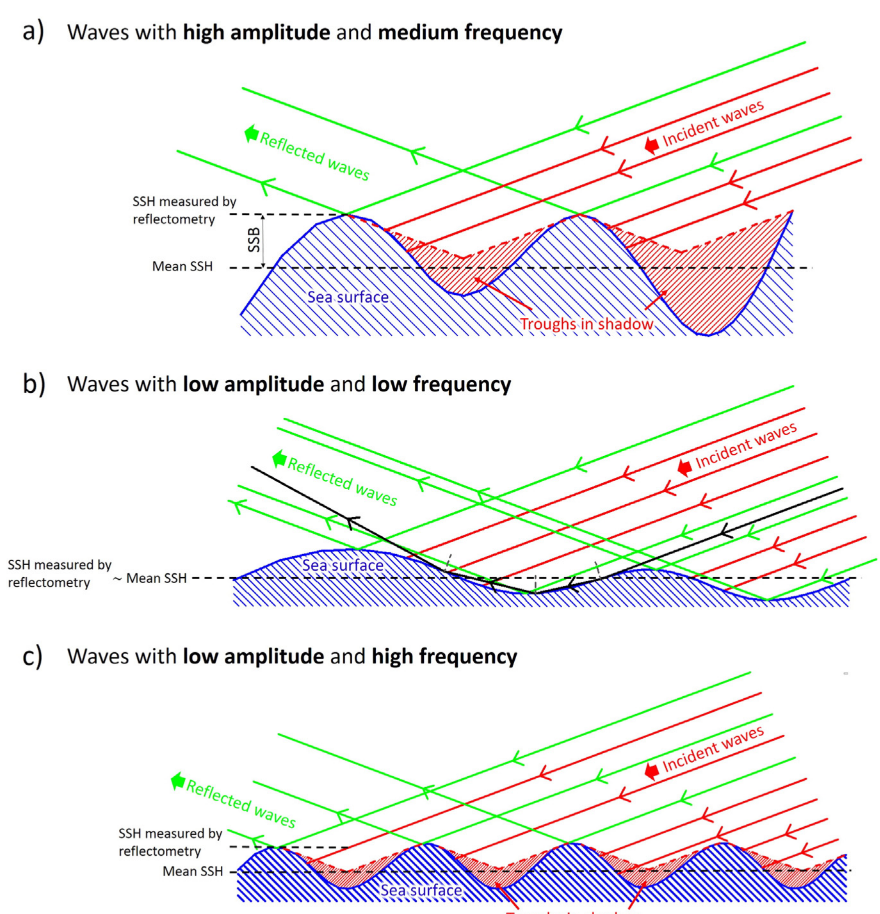

Fig. 13. Sea State Bias (SSB) induced by waves troughs shadowing when measuring off-nadir at low elevation angles with high amplitude and frequency of waves (a) or low amplitude but high frequency of waves (c). Signal convergence in troughs with low amplitude and frequency of waves (b). SSH: Sea Surface Height.

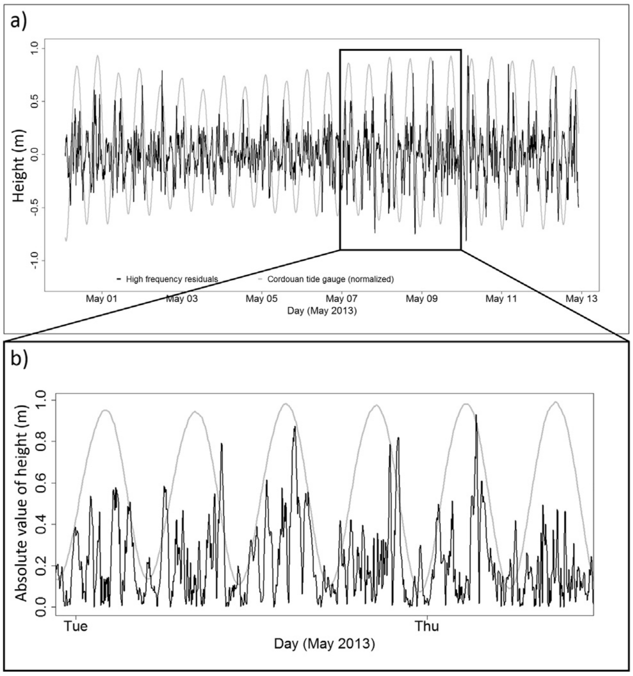

Fig. 14. High frequency signal extracted from raw SNR-based time series and Cordouan tide gauge (normalized), from 29 April to 13 May 2013, with δt = 4000s.

the series used for validation. Some noisy periods are also visible below 6 hours, particularly at 3 and 1.5 hours.

A wavelet cross correlation was computed between raw SNR-based time series and T-UGOm/Port-Bloc records and results are presented in Fig. 11. The wavelet cross correlation transform was also performed between Port-Bloc and T-UGOm time series in order to validate the comparison with the SNR-based one.

With regard to the T-UGOm versus Port-Bloc time series, the 6-, 12- and 24-hour periods are clearly seen, which is also the case with the comparisons versus raw SNR-based time series. The main astronomical periods are thus perfectly described by the SNR-based tide gauge.

Periods lower than 6 h are also present in the wavelet cross correlation between the classical tide gauge versus the raw SNR-based time series, particularly at 3 h.

The mean time shift for the 12 h-period over the whole period is equal to 3.6 minutes between T-UGOm and SNR time series; 27.8 minutes between Port-Bloc and SNR time series; 31.4 minutes between Port-Bloc and T-UGOm time series; 24.3 minutes between Royan and SNR time series; 27.9 minutes between Royan and T-UGOm time series and 3.5 minutes between Royan and Port-Bloc time series.

Table 7
Comparisons between the classical SNR analysis method and our method with respect to Cordouan tide gauge records from 28 April to 13 May 2013.

Cordouan compared to	Classical method	Our method
R	0.82	0.97
R^2	0.67	0.95
RMSE	1.52	0.63
Bias	0.22	0.01

These values are very close to the shifts obtained previously to reach the best linear correlation (§4.1.1) which was expected by assuming that the 12 h-period is the strongest one (see Table 2).

Fig. S3 presents the wavelet cross correlation between raw SNR-based data/Royan and Port-Bloc tide gauge records.

5.3. Detection of waves

5.3.1. Impact of the waves on the sea surface height (SSH)

If SNR-based time series of water levels provides a very good estimates of the tides (e.g. linear correlation equal to 0.97 with Cordouan tide records), RMSE remains quite high (e.g. 0.63 m with Cordouan tide gauge) and amplitude of the SNR-based time series is generally much higher than the other tide gauge data. This is clearly visible in Fig. 12 for the two-week period of common availability of SNR and Cordouan tide gauge records. As highlighted in this figure, SNR-based sea level variations are higher than Cordouan tide records at high tides but the difference is not constant.

The SNR-based water levels estimates are likely to be impacted by waves, that is not the case for the Cordouan tide gauge which is protected against this effect by the action of a dampener. Interaction between the electromagnetic waves and the waves tend to bias the estimate of SSH. This effect, known as Sea State Bias (SSB), is commonly taken into account when estimating SSH from radar nadir-looking altimetry measurements (e.g. Chelton et al. (2001)). Most of the power received by the altimeter comes from trough hence causing an underestimate of the SSH. In our case, the measurements are off-nadir and more significant results given by LSP are for low satellites elevation angles (reflected signal perturbations are mainly visible for low satellites elevation angles, see Section 2.2). Two extreme scenarios are thus possible:

- *waves with high amplitude and frequency*: the phenomenon is thus inverse to what occurs with nadir measurement: the major part of the received signal comes from the wave crests which hide the troughs,

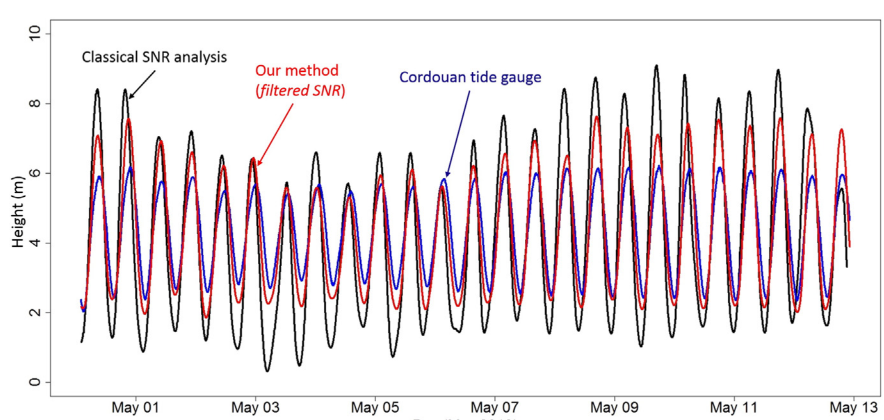

Fig. 15. SNR-based tide measurements obtained with classical SNR analysis (black line) compared with our method (red line) and co-located Cordouan tide gauge (blue line), from 28 April to 13 May 2013. (For interpretation of the references to color in this figure legend, the reader is referred to the web version of this article.)

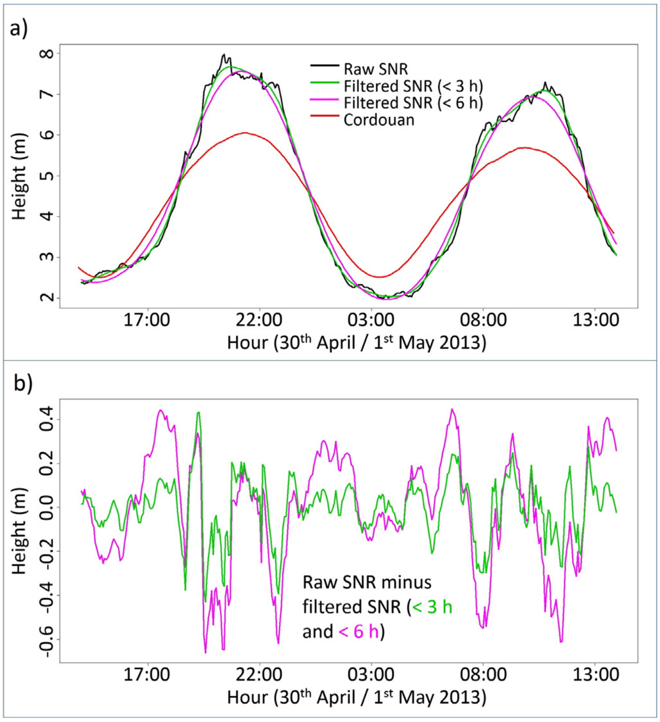

Fig. 16. Effects of the low-pass filtering of the raw SNR-based time series. (a) Zoom on the time series of the Cordouan tide gauge records (red line) and raw SNR-based tide (black line) to which is applied a 3 and 6 h low pass filter (green and purple lines respectively). (b) Differences between raw SNR-based time series and filtered SNR-based time-series.

as illustrated in Fig. 13 a. As a consequence, GNSS-R measurements will tend to measure the wave crests when their amplitude and, above all, frequency are high. Bias will thus be close to SWH which is the average of the highest third of the waves amplitude.

- *waves with low amplitude and frequency*: GNSS waves can reflect both on crests and troughs and measured sea level will be similar to mean sea level measured by classical tide gauge, as illustrated in Fig. 13 b. If waves amplitude and frequency are sufficiently low, the GNSS electromagnetic waves are mostly reflected in the troughs, causing a negative bias similar to the classical SSB in ssnadir-altimetry. In that case, GNSS-R tends to measure troughs and measured sea level will be lower than classical tide gauge records.

Intermediate cases are also possible, for instance considering waves with low amplitude but high frequency. This case leads to an over-determination of the SSH, as illustrated in Fig. 13 c.

To verify our assumption, the SWH from Wave Watch III model was added to the Cordouan tide records compared to the SNR-derived water levels. The result is presented in Fig. 12. During high tides, SNR-based time series and Cordouan tide gauge records plus SWH are generally in very good agreement except for some events during high tides (e.g., the 28 April, 4 May and 6 May 2013), which can be accounted for by the coarse resolution of the wave model (0.5°) that is not adapted for coastal areas and estuaries. Moreover, the Wave Watch III model does not integrate the strong breaking of waves caused certainly by a coarse bathymetry close to the coastal and estuary areas.

Table 8
Comparisons between the filtered SNR-based time series and the Cordouan tide gauge records from 28 April to 13 May 2013.

Threshold of the low-pass filter (h)	Bias	*R*	R^2	*RMSE*
0	0.01	0.956	0.913	0.774
3	0.01	0.962	0.925	0.742
6	0.01	0.972	0.946	0.632

With regard to low tides, SNR-based values and Cordouan tide records are similar when SWH is high (≥1 m). It is explained by the fact that waves amplitude decrease as the tide recedes (see Section 4.1), hence SSB value tends to zero. In this area, wave amplitudes are high during high tides. At low tides, the surface around the lighthouse is less rough due to both the presence of sandbanks and a smoother sea surface (lighthouse guards personal communication). SNR-based SSH is thus equal to tide gauge records. When waves amplitude is sufficiently low (SWH below s ~ 1 m), SNR-based SSH is lower than tide gauge records, which confirms our assumption that GNSS electromagnetic waves are mostly reflected in wave troughs with possibility of more than one multipath (dark path in Fig. 13 b). An almost constant minimal value around 2.3 m can also be observed in the SNR-based time series. It is due to the presence of sandbanks appearing in the whole area covered by reflection at low tides (see Figs. 6 and 5). It is interesting to stress out that sandbanks slightly move between each tide hence little differences over time.

5.3.2. Sea state

The remaining high-frequency signal from the low-pass filter applied to the raw SNR-based time series is plotted on Fig. 14.

Mean amplitude of this high-frequency signal is of 17 cm, and can reach 93 cm. As presented in Section 3.6, altimetric accuracy of the method is better than decimetric. The origin of this high-frequency signal cannot be attributed to noise, but most likely to a geophysical phenomenon. Amplitudes are generally high during high tides and below 30 cm during low tides (Fig. 14 b), which leads us to think that waves are at the origin of these perturbations. Indeed, as discussed in Section 5.3.1, highest amplitudes of waves are reached during high tide periods, and the sea surface is smoother during low tide periods and we recall to the reader that during high tides, the crests of the waves are more likely to be detected (see §4.3.1).

We estimated the mean amplitude of the high-frequency signal during each high tide period (i.e. during the time intervals where Cordouan tide gauge records were higher than the mean tide value over the two-week period). Linear correlation between the resultant time series and SWH from Wave Watch III model outputs is 0.60, which corroborates the assumption that waves are likely at the origin of this high-frequency component.

5.4. Comparison with the classical SNR analysis method

We finally compared the results from the dynamic SNR method with the ones obtained using the classical SNR analysis method. We recall here the major differences between the two methods:

- classical SNR analysis neglects $\dot{h}$, the variations of h against time, in Eq. (5);
- in classical SNR analysis, inversion is performed individually for every satellite data (with elevation angle below 40°);

We applied classical SNR analysis method over 28 April to 13 May 2013 using the same moving average (4000 s) and sampling rate (5 min) as for the new method, and we filtered out high frequency components (period higher than 6 h) in both cases.

Fig. 15 and Table 7 show the results obtained over the 15 days period. Linear correlation between classical SNR analysis results and Cordouan tide gauge is 0.82, i.e. 0.15 lower than with the dynamic SNR method (0.97), and RMSE is almost 2.5 times higher.

5.5. Effects of the filtering of the raw SNR-based time series

A low-pass filter was applied to the raw SNR-based time series in order to remove the high frequency signals considered as noise when determining the main astronomical tide periods (see §2.5). The consequences of such a filtering were tested on the two-week common period of SNR measurements and Cordouan tide gauge records, and results are visible in Fig. 16 and Table 8. By applying a 6 h low-pass filter, bias remains unchanged, and the linear correlation with Cordouan tide gauge records over the two-week period increases from 0.96 to 0.97. RMSE of the raw SNR-based time series is 0.77, while it is 0.74 by applying a 3 h low-pass filter, and 0.63 with a 6 h low-pass filter.

6. Conclusion

In this study, a new inversion technique of the SNR measured using a single geodetic GNSS receiver for retrieving sea surface height and its variations versus time was developed. It offers a significant improvement of the classical SNR analysis method (Larson et al., 2013) by taking the dynamics of the reflecting surface into account. The method proposed in this study allows the use of the SNR-based altimetry even if the variations against time of the reflecting surface are not negligible. Residuals in the altimetric results are related to the changing significant wave height. Our dynamic SNR method was validated with SNR data collected from a GNSS antenna set up at the top of a 60-meter high lighthouse, 8 km from the Shore. Comparisons with in situ data from tide-gauges show a very good agreement: linear correlation versus time with classical tide gauges is better than 0.92 (0.94 when high frequencies caused by waves are filtered out) over a 3-month period of measurement. It reaches 0.97 (0.96 without removing high-frequency signal) with a co-located tide gauge over a 2-week period, while it only reaches 0.82 using the classical method. RMSE is about 0.63 m (respectively 0.77 m) while it is almost 2.5 times higher with the classical method. The high values of RMSE can be explained by the wave signals present in our SNR-based estimates and not in tide gauge records used for validation as they are protected against wave effects by the action of a dampener, and the emergence of sandbanks around the lighthouse as the tide recedes. That affect our determination of sea surface height but not the classical tide gauges. The higher the GNSS receiver is, the larger the study area is. As a consequence, the estimates are also affected by the spatial inhomogeneities of the surface height around the lighthouse.

Our dynamic SNR method of inversion of GNSS SNR data demonstrated a strong potential for the monitoring of SSH in coastal areas especially in areas with high tides and our comparisons with independent sources of tide measurements reveal that, concerning the main tide periods of ~6 h, ~12 h and ~24 h, our SNR-based tide gauge provides results of similar quality to the classical tide gauges.

Our inversion technique being based on the resolution of an overdetermined system, the more satellites in sight, the more accurate the method will be. With the advent of the new GNSS constellations (GALILEO, COMPASS-Beidou, etc.), the accuracy and temporal resolutions of the method is likely to be improved in the future. The dynamic SNR method also demonstrated a strong consistency in the determination of swell as the residuals between our estimates and the tide gauge records exhibit similar temporal variations as the swell from the WaveWatch III model. Its range of applicability should nevertheless be limited to low altitude receivers. First because a too large antenna height above the reflecting surface would induce a too small time period of the SNR variations to be measurable with a classical 1 Hz acquisition. Secondly, because reflections from higher altitudes over open waters might start behaving as mostly diffuse, not coherent. And last, C/A code having ~300 m chip length, any relative reflect-to-direct distance larger than that would not induce interferences. Conversely, the lower the antenna height is, the lower the frequency of the SNR variations is, hence worse temporal resolution in the final sea level determination.

Acknowledgments

This work was funded by CNES in the framework of the TOSCA project "Hydrologie, Océanographie par Réflectométrie GNSS (HORG)" and by the RTRA STAE Foundation in the framework of the "Potentialités de la Réflectométrie GNSS In Situ et Mobile (PRISM)" project. Nicolas Roussel is supported by a PhD granted from Ministère de l'Enseignement Supérieur et de la Recherche (MESR). We thank the GPMB, and especially A. Fort, for providing us with the tide gauge records from Cordouan station. Particular thanks are also addressed to the *Subdivision des Phares et Balises* and to the *Syndicat Mixte pour le Développement de l'Estuaire de la Gironde* (SMIDDEST) for having allowed us to install our GNSS receiver at the top of the Cordouan lighthouse and the lighthouse guardians for their kind and useful help. Last, we also thank B. Meyssignac (LEGOS-OMP, CNES) for the fruitful discussions. Crosswavelet coherence software and wavelet coherence software were provided by A. Grinsted.

Appendix A. Supplementary data

Supplementary data to this article can be found online at http://dx.doi.org/10.1016/j.rse.2015.10.011.

References

Ablain, M., Cazenave, A., Valladeau, G., & Guinehut, S. (2009). A new assessment of the error budget of global mean sea level rate estimated by satellite altimetry over 1993–2008. *Ocean Science*, *5*(2), 193–201.

Anderson, K. (1995). A GPS tide gauge. *GPS World Showcase*, *6*.

Bilich, A. (2006). *Improving the precision and accuracy of geodetic gps: Applications to multipath and seismology.* (PhD thesis) University of Texas at Austin. M.S., University of Colorado.

Bishop, G., & Klobuchar, J. (1985). Multipath effects on the determination of absolute ionospheric time delay from GPS signals. *Radio Science*, *20*(3), 388–396.

Bouffard, J., Roblou, L., Birol, F., Pascual, A., Fenoglio-Marc, L., Cancet, L., ... Ménard, Y. (2011). *Introduction and Assessment of Improved Coastal Altimetry Strategies: Case Study Over the Northwestern Mediterranean Sea.* Berlin Heidelberg: Springer, 297–330.

Butterworth, S. (1930). On the theory of filter amplifiers. *Wireless Engineering*, *7*, 536–541.

Cardellach, E., Ao, C., de la Torre Juarez, M., & Haji, G. (2004). Carrier phase delay altimetry with GPS-reflection/occultation interferometry from low earth orbiters. *Geophysical Research Letters*, *31*(10).

Cardellach, E., Fabra, F., Noguès-Correig, O., Oliveras, S., Ribo, S., & Rius, A. (2011). GNSS-R ground-based and airborne campaigns for ocean, land, ice, and snow techniques: Application to the gold-RTR data sets. *Radio Science*, *46*(RS0C04).

Carreno-Luengo, H., Camps, A., Ramos-Perez, I., & Rius, A. (2014). Experimental evaluation of gnss-reflectometry altimetric precision using the p(y) and c/a signals. *IEEE Journal of Selected Topics in Applied Earth Observation Remote Sensing*, *7*(5), 1493–1500.

Chelton, D., Ries, J., Haines, B., Fu, L., Callahan, P., Fu, L. -L., & Cazenave, A. (2001). Satellite altimetry. *Satellite altimetry and the earth sciences: A handbook of techniques and applications* (pp. 1–131). Academic Press.

Cohen, J., Small, C., Mellinger, A., Gallup, J., Sachs, J., Vitousek, P., & Mooney, H. (1997). Estimates of coastal populations. *Science*, *278*(5341), 1209–1213.

Duraiappah, A., Naeem, S., Agardy, T., Ash, N., Cooper, H., Diaz, S., ... Van Jaarsveld, A. (2005). *Ecosystems and human well-being: Biodiversity synthesis.* Coastal Systems.

Georgiadou, Y., & Kleusberg, A. (1988). On carrier signal multipath effects in relative gps positioning. *Manuscripta Geodaetica*, *13*, 172–179.

Grinsted, A., Moore, J., & Jevrejeva, S. (2004). Application of the cross wavelet transform and wavelet coherence to geophysical time series. *Non Linear Processing Geophysics*, *11*.

Hannah, B. (2001). *Modelling and simulation of gps multipath propagation.* (PhD Thesis) Queensland University of Technology.

Larson, K., Löfgren, J., & Haas, R. (2013). *Journal of Advances in Space Research*, *51*(8), 1301–1310.

Larson, K., Small, E., Gutmann, E., Bilich, A., Axelrad, P., & Braunn, J. (2008). Using GPS multipath to measure soil moisture fluctuations: Initial results. *GPS Solutions*, *12*, 173–177.

Le Traon, P., Morrow, R., & Cazenave, A. (2001). Coastal sea level measurements using a single geodetic GPS receiver. In L. -L. Fu (Ed.), *Satellite altimetry and earth sciences. A handbook of techniques and applications* (pp. 171–215). San Diego, USA: Academic.

Löfgren, J. (2014). *Local sea level observations using reflected GNSS signals.* (PhD Thesis) Department of Earth and Space Sciences. Chalmers University of Technology.

Löfgren, J., & Haas, R. (2014). Sea level measurements using multi-frequency gps and glonass observations. *EURASIP Journal on Advances in Signal Processing*, *2014*(1), 1687–6172.

Löfgren, J., Haas, R., & Scherneck, H. (2014). Sea level time series and ocean tide analysis from multipath signals at five GPS sites in different parts of the world. *Journal of Geodynamics*, *80*, 66–80.

Löfgren, J., Haas, R., Scherneck, H., & Bos, M. (2011). Three months of local sea level derived from reflected GNSS signals. *Radio Science*, *46*(RS0C05).

Lomb, N. (1976). Least-squares frequency analysis of unevenly spaced data. *Astrophysical and Space Science*, 447–462.

Lowe, S., Zuffada, C., Chao, Y., Kroger, P., Young, L., & LaBrecque, J. (2002). 5-cm-precision aircraft ocean altimetry using GPS reflections. *Geophysical Research Letters*, *29*(1375).

Lyard, F., Lefevre, F., Letellier, T., & Francis, O. (2006). Modelling the global ocean tides: Modern insights from FES2004. *Ocean Dynamics*, *56*, 394–415.

Martin-Neira, M. (1993). A passive reflectometry and interferometry system (paris): Application to ocean altimetry. *ESA Journal of the European Space Agency*, 331–355.

Millar, D., Smith, H., & Reeve, D. (2007). Modelling analysis of the sensitivity of shoreline change to a wave farm. *Ocean Engineering*, *34*(5–6), 884–901.

Nicholls, R., Wong, P. P., Burkett, J., Codignotto, J., Hay, R., McLean, S., ... Woodroffe, C. (2007). *Coastal systems and low-lying areas. climate change 2007: Impacts, adaptation and vulnerability. contribution of working group ii to the fourth assessment report of the intergovernemental panel on climate change.* Cambridge University Press, 315–357.

Rius, A., Noque's-Correig, O., Ribo, S., Cardellach, E., Oliveras, S., Valencia, E., ... Martin-Neira, M. (2012). Altimetry with gnss-r interferometry: first proof of concept experiment. *GPS Solutions*, *16*, 231–241.

Roussel, N., Frappart, F., Ramillien, G., Desjardins, C., Gegout, P., Pérosanz, F., & Biancale, R. (2014). Simulations of direct and reflected waves trajectories for in situ GNSS-R experiments. *Geoscientific Model Development*, *7*, 1001–1062.

Ruf, T. (1999). The lomb-scargle periodogram in biological rhythm research: Analysis of incomplete and unequally spaced time-series. *Biological Rhythm Research*, *30*(2), 178–201.

Ruffini, G., Soulat, F., Caparrini, M., Germain, O., & Martin-Neira, M. (2004). The eddy experiment: Accurate gnss-r ocean altimetry from low altitude aircraft. *Geophysical Research Letters*, *31*(L12306).

Scargle, J. (1982). Studies in astronomical time series analysis. II — Statistical aspects of spectral analysis of unevenly sampled data. *Astronomy Journal*, *263*, 835–853.

Semmling, A., Beyerle, G., Stosius, R., Dick, G., Wickert, J., Fabra, F., ... d'Addio, S. (2011). Detection of artic ocean tides using interfeometric GNSS-R signals. *Geophysical Research Letters*, *38*(L04103).

Semmling, A., Schmidt, T., Wickert, J., Schön, S., Fabra, F., Cardellach, E., & Rius, A. (2012). On the retrieval of the specular reflection in GNSS carrier observations for ocean altimetry. *Radio Science*, *47*(RS6007).

Stammer, D., Ray, R., Andersen, O., Arbic, B., Bosch, W., Carrère, L., ... Yi, Y. (2014). Accuracy assessment of global barotropic ocean tide models. *Reviews of Geophysics*, *52*(3), 243–282.

Taylor, C., Pedregal, D., Young, P., & Tych, W. (2006). Environmental time series analysis and forecasting with the captain toolbox. *Environmental Modelling and Software*, *22*, 797–814.

Tolman, H. (2014). *User manual and system documentation of wavewatch-III version 4.18. NOAA/NWS/NCEP/OMB technical note 316.*

Treuhaft, R., Lowe, S., Zuffada, C., & Chao, Y. (2001). Two-cm GPS altimetry over crater lake. *Geophysical Research Letters*, *28*(23), 4343–4346.

UN (2010). Atlas of the Oceans: Human Settlements On the Coast. (available on: www.oceanatlas.org/servlet/CDSServlet?status=ND0xODc3JjY9ZW4mMzM9KiYzNz1rb3M.).

Young, P. (2001). Data-based mechanistic modelling and validation of rainfall-flow processes, model validation: perspectives. *Hydrological Science*, 117–161.

Yu, K., Rizos, C., & Dempster, A. (2014). Gnss-based model-free sea surface height estimation in unknown sea state scenarios. *IEEE Journal of Selected Topics Applied Earth Observation Remote Sensing*, *7*(5), 1424–1435.